UNIVERSITY OF CALIFORNIA,
IRVINE

Utilizing Microphysiological Platforms to Interrogate Inflammatory Disease Conditions: Modeling SARS-CoV-2 and Atherogenesis

DISSERTATION

submitted in partial satisfaction of the requirements
for the degree of

DOCTOR OF PHILOSOPHY

in Pharmaceutical Sciences

by

Sebastian Duncan Piombo

Dissertation Committee:
Professor Dan Cooper, Chair
Professor Christopher C.W. Hughes
Associate Professor Shlomit Radom-Aizik
Associate Professor Naoto Hoshi

2023

DEDICATION

To my educators—
past, present, and future

My gratitude for your time and knowledge is boundless.

TABLE OF CONTENTS

LIST OF FIGURES

ACKNOWLEDGEMENTS

I would like to thank my committee chair, Professor Dan Cooper, for his keen insights, unquenchable curiosity, and unflagging kindness. Your passion in the pursuit of knowledge for the betterment of the human condition provides the bedrock for my aspirations to provide care as a physician-scientist. I would also like to thank Professor Christopher Hughes, who has adopted me into his lab and provided the innovation and bounty of practical insight that has allowed for a physician-scientist trainee to partake in true translational research. My gratitude extends to Professor Shlomit Radom-Aizik, who has not just guided me since my very first days as a graduate student but made me feel like I have a family in science. And to Professor Naoto Hoshi, whose teachings set me on the path towards a degree in Pharmaceutical Sciences.

My thanks to my co-author and friend Christopher Hatch, who has provided computational knowledge beyond reproach and been a stalwart presence and asset in the development of our COVID-19 research.

I would also like to thank my labmates, of whom there are many. It takes a village to find success in science, and I thank you all not just for your valued thoughts, opinions, and technical knowledge but for providing the ineffable social fabric that allows us to persevere through failure.

I am grateful for funding support provided by the University of California, Irvine Medical Scientist Training Program, as well as our COVID funding source from our 5T32HL116270-08 grant from the National Heart, Lung, and Blood Institute.

Finally, a thank you beyond measure to my wife Gabrielle Piombo. We have faced profound trials and tribulations during my graduate study years; your unflappable support and love has been instrumental in all my successes.

VITA
Sebastian Duncan Piombo

2015	B.S. in Chemistry, New York University
2015-2017	MS1-MS2, University of California, Irvine
2023	Ph.D. in Pharmaceutical Sciences, University of California, Irvine

FIELD OF STUDY

Translational Research Application of Microphysiological Systems

PUBLICATIONS

Wagh, V., Pomorski, A., Wilschut, K. J., **Piombo, S**., & Bernstein, H. S. (2014). MicroRNA-363 negatively regulates the left ventricular determining transcription factor HAND1 in human embryonic stem cell-derived cardiomyocytes. *Stem cell research & therapy*, *5*(3), 1-10.

Brady, M., **Piombo, S**. D., Hu, C., & Buccella, D. (2016). Structural and spectroscopic insight into the metal binding properties of the o-aminophenol-N, N, O-triacetic acid (APTRA) chelator: implications for design of metal indicators. *Dalton Transactions*, *45*(31), 12458-12464.

Rojanasopondist, P., Nesheiwat, L., **Piombo, S.**, Porter Jr, G. A., Ren, M., & Phoon, C. K. (2022). Genetic basis of left ventricular noncompaction. *Circulation: Genomic and Precision Medicine*, *15*(3), e003517.

ABSTRACT OF THE DISSERTATION

Utilizing Microphysiological Platforms to Interrogate Inflammatory Disease Conditions:
Modeling SARS-CoV-2 and Atherogenesis

by
Sebastian Duncan Piombo
Doctor of Philosophy in Pharmaceutical Science
University of California, Irvine, 2023
Professor Dan Cooper, Chair

One of the pressing concerns in translational and clinical research is the development of accurate model systems that allow scientists to recapitulate the native tissue and organ systems vulnerable to disease. Barring direct human experimentation, one of the great challenges of translational research is drawing parallels between a human condition and an appropriate and available model. To address this conundrum, researchers have painstakingly developed a wide range of animal models and creative uses of cell culture to attempt to draw closer comparisons to that of actual human organ systems. While this variety of model options narrows the gap between a human condition and what is observable in a laboratory setting, unfortunately discrepancies remain. The primary objective of the work presented here is to develop novel technologies that enable an accurate representation of a specific target organ system and to apply said technology to study the pathogenesis of two human diseases centered on immune dysregulation, namely COVID-19 and early-stage cardiovascular disease.

The advent of microphysiological systems enables the high-throughput study of self-contained, human derived, three-dimensional tissue samples *in vitro* to provide a range of organ models that can be curated to address specific questions in the study of human diseases. This work focuses on the utilization of two distinct vascular microphysiological systems to study two of the most urgent public health concerns in both the United States and globally. Both COVID-19 and the beginning of cardiovascular disease, atherogenesis, are driven by immune dysregulation and subsequent damage to the vascular system. The two platforms utilized in this work, the vascularized micro-organ and the single channel arteriole, are based off the same

principal concept of loading a population of stromal cells and endothelial cells into a polydimethylsiloxane chamber and allowing the resultant vascular tissue to develop under flow conditions. The use of the vascularized micro-organ has allowed us to study both the immediate and downstream inflammatory effects of SARS-CoV-2 infection on a human vascular system while the development of the higher shear single channel arteriole provides insight into the cell-to-cell interactions that initiate the first stage of cardiovascular disease.

Chapter 1:
Flow-induced ACE2 expression allows for SARS-CoV-2 infection of endothelial cells in a vascularized microphysiological system

Abstract

Severe acute respiratory syndrome coronavirus 2 (SARS-CoV-2), the virus that causes coronavirus disease 2019 (COVID-19), has resulted in nearly 7 million deaths to date globally. Severe COVID-19 is associated with a hyperaggressive inflammatory response characterized by hypercytokinemia (i.e. “cytokine storm”) and endothelial damage. the development of a vaccine for SARS-CoV-2 has reduced hospitalization rates, but hypercytokinemia remains a major concern among those with breakthrough infections leading to severe COVID-19. This suggests that disease models that recapitulate the COVID-19 hypercytokinemia response are still necessary. Our lab has previously developed a vascularized micro-organ (VMO) microphysiological system that supports de novo formation of a perfused and physiological microvasculature. Here, we adapt the VMO to model endothelial dysfunction following SARS-CoV-2 infection. We find that expression of renin-angiotensin signaling axis components, which mediate SARS-CoV-2 cell entry, is preserved in endothelial cells in the VMO compared to 2D monolayer. Additionally, we show that SARS-CoV-2 pseudovirus has increased infectivity in the VMO compared to in monolayer, and that exposure of the VMO to SARS-CoV-2 pseudovirus reduces ACE2 expression while increasing key pro-inflammatory markers. Perfusion of recombinant Angiotensin II (rAng II) through the VMO mimics SARS-CoV-2 infection suggesting enhanced renin-angiotensin signaling may contribute to endothelial dysfunction in COVID-19.

Introduction

The SARS-CoV-2, or COVID-19, pandemic has required major adaptations in how the medical and scientific community approaches infectious disease prevention and study (Xiao, 2020; Kluge, 2020). One of the primary needs has been the rapid development of new tools to analyze viral infection and the subsequent development of vaccines to combat the global dissemination of this deadly pathogen (Le, 2020). To address the dearth of apt translational models for studying the pathogenesis of COVID-19, we have utilized a 3D microphysiological system (MPS) platform – the vascularized micro-organ (VMO) model – to interrogate the role of the vasculature in driving hypercytokinemia, which is a key pathological indicator associated with SARS-CoV-2 infection (Tang, 2020).

While COVID-19 was initially characterized as an infection that predominately manifests in the respiratory system, it is now also recognized to also be a vascular disease (Potus, 2020), with potential long-term sequalae likely arising due to micro-clots associated with dysregulation of thrombosis in many patients (Roberts, 2020). While the long-term effects of COVID-19 infection appear to be mediated by these thrombotic events, the most severe acute impact of the disease is driven by profound hypercytokinemia; a process associated with uncontrolled upregulation of key inflammatory mediators such as IL-1 and IL-6, and endothelial cell (EC) leukocyte adhesion molecules such as ICAM-1 and VCAM-1 (Hu, 2021; Copaescu, 2020). This cascading inflammatory response frequently results in pneumonia and, in severe cases, acute respiratory distress syndrome, accounting for the high mortality prior to the introduction of the COVID-19 vaccine (Gibson, 2020). Therapies such as glucocorticoids and antivirals such as remdesivir have been developed to combat these cases; however, the biological mechanisms that produce hypercytokinemia in COVID-19 patients remain elusive, although the use of tociluzumab, targeted to the IL-6 receptor, has proven useful in many patients (Rosas, 2021). To further our understanding of the pathology of COVID-19 and the role of the vasculature, we

have challenged our VMO platform with a non-replicative pseudotyped SARS-CoV-2 HIV virus allowing us to model and visualize viral entry into human EC in a system that closely recapitulates human vasculature. The VMO consists of human-derived primary EC and stromal cells, suspended in a hydrogel matrix housed within a polydimethylsiloxane microfluidic system. Over the course of a few days, a complex vascular network forms that is then perfused by a blood substitute, which nourishes the surrounding tissue. These microvascular networks demonstrate key characteristics of human vasculature, such as tight junctions, expression of vascular markers, and response to inflammatory stimuli, and can support a variety of tissues including heart, liver, pancreas, brain and various tumors (Phan, 2017; Hachey, 2018; Sobrino, 2016).

The key mediator of SARS-CoV-2 viral entry into host cells is angiotensin converting enzyme 2 (ACE2), which acts as a receptor for the viral spike protein (Davidson, 2020). While other renin-angiotensin system mediators, such as AGTR1, play a role in the resultant hypercytokinemia (Ramasamy, 2021), ACE2 expression on the surface of EC is critical to the initial infection, and without adequate expression viral infection fails to occur (Hamming, 2004). The primary challenge of studying SARS-CoV-2 infection in commonly utilized models of the vasculature is the dependence of ACE2 expression on the shear force EC are exposed to in vivo (Song, 2020; Kaneko, 2020). The VMO provides flow and shear force equivalent to that found in human capillary networks, roughly 2-2.5 dynes/cm^2 on the lower end. Thus, the VMO provides a unique platform in which to study not only how ACE2 mediates viral infection, but also how viral entry clears ACE2 from the surface of the EC lining the vascular network.

Methods

Microfluidic Device Design

The design of the platform is a modified version of our previously published VMO microphysiological system (Phan, 2017; Moya, 2013). The platform is designed to fit a standard bottomless 96-well plate (FLUOTRAC™, Greiner Bio-One). The design is shown in Fig 1A and comprises two polydimethylsiloxane (PDMS) layers adhered to a commercial 96-well plate with the wells aligned with the microfluidic features. The roughly 2 mm thick middle layer contains 16 microfluidic device units within the PDMS device layer, and the bottom layer is a thin transparent polymer membrane (Rogers Corp, HT-6240).

A single microfluidic device unit covers six horizontal wells of the 96-well plate, with the tissue chamber containing three diamond-shaped units (T1-T3) covering one well. A gel loading inlet (GLI) and outlet (GLO) are connected to either side of the tissue chamber, and each is aligned with an additional well. Each diamond-shaped unit is 2 mm in length and 1 mm in width, connected to 200 μm wide microfluidic channels through anastomosis points. The entire design is 200 μm thick. A redundant gel outlet is integrated into the GLI1 to act as a pressure regulator (PR) and prevent hydrogel from entering the microfluidic channel when the loading pressure exceeds the anastomosis point burst valve pressure. The microfluidic channels contain resistors in an asymmetric design to generate a hydrostatic pressure drop across the tissue chamber. This drives interstitial flow as the medium moves from the medium inlet (MI) to the medium outlet (MO).

Microfluidic Device Fabrication

The fabrication of the VMO has been previously described (Hachey, 2018; Sobrino, 2016; Phan, 2017). Briefly, a customized polyurethane (PU) master mold is fabricated from a two-part PU liquid plastic (Smooth-Cast 310, Smooth-On Inc.). A PDMS replica is made from the master mold, and holes are punched on the replica for the inlets and outlets (MI, MO, GLI1, GLO1, PR). The replica is secured to the bottom of a 96-well plate by chemical glue and oxygen plasma treatment. The bottom thin transparent membrane is bonded to the PDMS layer with oxygen plasma treatment. The complete platform is placed in a 60°C oven overnight. Before the platform is loaded with cells, a standard 96 well-plate polystyrene lid with condensation rings (Greiner Bio-One) is placed on top, and both parts are sterilized using a UV light for 30 minutes.

Cell Culture

Human endothelial colony-forming cell-derived endothelial cells (ECFC-EC) were isolated from cord blood (Melero-Martin, 2008), expanded on 0.1% gelatin-coated flasks, and cultured in EGM-2 (Lonza). ECFC-EC were transduced with lentiviruses encoding azurite fluorescent protein (Azurite/Addgene) and used between passages 7-9. Note that images are false-colored so that EC appear red. Normal human lung fibroblasts (NHLF) (Lonza) were cultured in DMEM (Corning) containing 10% FBS (VWR) and used between passages 7-10. All cells were cultured at 37°C/20% O_2/5% CO_2 and checked for mycoplasma contamination using MycoAlert (Lonza) before use.

Microfluidic Device Loading

The tissue chamber was loaded with ECFC-EC and NHLF. The cells were trypsinized, lifted, and resuspended at a 1.4:1 ratio at a density of 1.4 x10^6 cells/mL in an 8 mg/mL fibrinogen solution (Sigma-Aldrich). Next, the cell-matrix solution was mixed with 3 U/mL

thrombin (Sigma-Aldrich) and loaded in the tissue chambers. The VMO was placed into a 37°C incubator for 15 minutes to enable polymerization of the cell-matrix mix. Next, laminin (1 mg/mL, Life Technologies) was pushed through the microfluidic channels and incubated for 15 minutes at room temperature. Finally, EGM-2 culture medium (Lonza) was pushed through the microfluidic channels and dispensed in the inlet and outlet wells to generate hydrostatic pressure heads that drive perfusion. Medium was changed every day to maintain the pressure heads.

Fluorescence Imaging and Analyses

Fluorescence images were captured on an Olympus IX70 inverted microscope using SPOT software (SPOT Imaging), and a Nikon Ti-E Eclipse epifluorescent microscope with a 4xPlan Apochromat Lambda objective. In addition, confocal images were captured on a Leica TCS SP8 confocal microscope using a standard 10x air or 20x multi-immersion objective (Leica Microsystems).

FIJI (Schindelin, 2012) was used to determine each microfluidic unit's mean fluorescent intensity (MFI). Before measuring the average pixel intensity, all images underwent thresholding and default background subtraction with the same setting using a custom macro. Then, for analysis, all values were normalized to the mean control fluorescent intensity.

Perfusion Testing

To test the vascular leak of device networks, 70kDa FITC-dextran (Sigma-Aldrich) was diluted in EGM-2 at a ratio of 1:100 and added to well MI for perfusion through the device. Images were taken after 15 minutes, and the vessel patency was assessed by demonstrating dextran flow through the entirety of the vascular chamber.

Generation of Pseudotyped SARS-CoV-2 Virus and Infection of the Microfluidic Device

Pseudotyped SARS-CoV-2 virions were generated by co-transfecting 1.5 x 10^7 293-T cells with a single round infectious HIV-1 NL4-3 Gag-iGFP ΔEnv plasmid as well as a SARS-CoV-2 spike protein expressing plasmid (pcDNA 3.1 SARS CoV-2 S). Plasmids (1 µg plasmid per 1 x 10^6 cells) were mixed with polyethylenimine (PEI) at a DNA/PEI ratio of 1:3 and added to the cells. After 3-4 days cell supernatants were harvested and cleared from cells. Virus aliquots were stored at -80ºC. To concentrate virus, frozen supernatants were thawed and spun (14,000 rpm) in a microcentrifuge for 75 min at 4ºC and viral pellets were resuspended in the respective medium. Virus infectivity was determined by infecting 1 x 10^4 human ACE2 receptor expressing HEK 293T target cells (BEI Resources) per well with a serial dilution of the CoV-2/HIV-1 pseudotyped virus particles. After 2 to 3 days, cells were detached, washed, and fixed with 4% PFA. Target cells were subsequently analyzed by flow cytometry (NovoCyte flow cytometer; ACEA) for green fluorescence protein expression. After performing perfusion tests to confirm the robustness of the vascular networks, the pseudotyped virus was added to the device inlet. To activate the renin-angiotensin system, recombinant angiotensin II (rAngII, Sigma-Aldrich, 4474-91-3) was added to the inlet at a 300 pM concentration. After 24 hours, medium heights were reestablished by taking the media from the outlet well and placing it back in the inlet. After 48 hours, the effluent was collected.

Immunostaining

VMO devices were perfusion fixed over-night at 4°C by replacement of circulating media in inlet and outlet reservoirs with 4% paraformaldehyde diluted in phosphate-buffered saline (PBS). Following fixation, the transparent polymer seal was removed exposing VMO networks embedded within the microfluidic feature layer, which was then placed face-up in each well of a 24-well plate. Fixed devices were then post-fixed for an additional 20 minutes in 4%

paraformaldehyde at room temperature and then incubated in blocking solution (PBS containing 3% bovine serum albumin (BSA) and 0.1% Triton X, supplemented with 1% donkey serum) for 1 hour at room temperature. Devices were then incubated in primary antibody diluted in staining solution (PBS containing 1% bovine serum albumin (BSA) 0.1% Triton X) overnight at 4°C. Following wash, devices were incubated in fluorescently conjugated secondary antibodies diluted in staining solution for 2 hours at room temperature, followed by incubation in 10ug/mL Hoechst 33342 (Sigma 14533) for 15 minutes at room temperature. Devices were then washed in PBS and mounted in 4-well glass chamber slides (Nunc Lab-Tek, Thermo 177399) in Vectashield (Vector Labs H1300) anti-fade mounting media. High magnification multi-channel images of stained VMO devices were acquired using a Leica SP8 confocal microscope. Primary antibodies used: anti-ACE2 (Novus NBP2-67692, 1:300), anti-TMPRSS2 (Abcam ab242384, 1:300), anti-CD31 (Abcam ab28364, 1:300). Fluorescently conjugated secondary antibodies used: anti-Rabbit-Alexa 488 (1:500), anti-mouse-Alexa 568 (1:500), anti-goat-Alexa 647 (1:500).

ELISAs

Effluent from devices was collected after 48 hours of exposure to experimental treatments. If not used immediately, the effluent was stored in the vapor phase of liquid nitrogen. Before use, the effluent was allowed to reach room temperature and was centrifuged at 2000g for 10 minutes. ELISAs for IL-6 (Abcam, ab178013), sICAM-1 (Abcam, ab229383), sVCAM-1 (Abcam, ab223591), Factor VIII (Abcam, ab272771), and IL-1β (Thermo Fischer Sci, BMS224-2) were run. A 100K molecular weight cutoff protein concentrator (Thermo Scientific, 88523) was used to pool two samples and concentrate them for the Factor VIII ELISA. The drc package (Ritz, 2015) in RStudio [Rstudio] was used to fit the standard data to point curves as the manufacturers' protocols recommended. Values that fell outside the range of the standards were excluded from the analysis.

RNA Isolation and qRT-PCR Analysis

For RNA isolation, the protective plastic cover underneath the platform was removed. A razor blade was used to extract the tissue chamber and surrounding chamber inlets and outlets. Carefully, tweezers were used to separate the bottom polymer layer from the PDMS layer. Approximately 20 µL of RNA lysis buffer from Quick RNA micro prep kit (Zymo Research, R1051) was added dropwise to the tissue chamber and bottom polymer layer and allowed to sit for 3-5 minutes. RNA lysis buffer was collected and diluted in a 1:1 ratio with pure ethanol before transfer to a Zymo-Spin IC Column. The RNA was then isolated following the manufacturer's protocol. The RNA was checked for quantity and quality using a NanoDrop before storage at -80 °C or immediate conversion into cDNA.

Total purified RNA was synthesized into cDNA with the iScript cDNA Synthesis Kit (BioRad, 1708891) before use in quantitative real-time polymerized chain reaction (qRT-PCR) (BioRad). The average cycle threshold values were normalized using 18S expression levels and then compared to their appropriate controls. All samples were measured in triplicate. Primers were designed with PrimerQuest Tool and synthesized by Integrated DNA Technologies.

Ibidi Chip

ECFC-EC were plated into the 0.4 mm µ-Slide I Luer (Ibidi, 80176) at $1x10^6$ cell/mL and 100 µL and allowed to adhere overnight following the manufacturer's protocol. Next, the cells were exposed to 4 hours of shear stress at either 0.5, 1.0, or 2.0 dynes/cm^2 using a syringe pump (Pump Systems Inc) with the flow rate set via ibidi's recommended values. After 4 hours, the chips were washed with DPBS 3X, and RNA lysis buffer using Quick RNA micro prep kit (Zymo Research, R1051) was pushed through the chamber following the manufacturer's protocol. As previously described, steps were followed to isolate the RNA and run qPCR.

Vessel Morphometry

Vascular network images were analyzed with AngioTool software (National Cancer Institute) to quantify vessel area, length, lacunarity, and the number of vascular junctions and endpoints. The mean vessel diameters were computed using a modified version of the REAVER package (Corliss, 2019) to output all vessel diameters instead of the mean for the entire network. The forked repository is available on GitHub (https://github.com/cjhatch/public_REAVER_diams).

NFκB Reporter and Monolayer Response

ECFC-EC were transduced with an NFκB reporter and plated into 12-well plates. mCherry expression was driven by NFκB expression in this line, allowing for indirect quantification of inflammatory status via fluoroscopy. 1.5 mL of effluent was collected from the VMOs and then layered onto the transduced EC. Each well was imaged at 0, 24, and 48 hours. MFI was calculated from each well to quantify the inflammatory response to downstream mediators.

Drug Treatments

After performing perfusion tests to confirm the robustness of the vascular networks, pharmacological agents were added at the same time as the pseudotyped virus to test their ability to limit infectivity. Recombinant ACE2 (25 μg/mL, Sigma-Aldrich, SAE0065-50UG) or camostat mesylate (100 μM, Sigma-Aldrich, SML0057-10MG) was premixed with medium +/- pseudotyped virus +/- rAngII for 30 minutes before perfusing through devices. The pressure heads were readjusted by recycling media from the outlet well back into the inlet after 24 hours, and effluent was collected after 48 hours. Images were taken at 0, 24, and 48 hours.

Computational Fluid Dynamics

Image masks were converted into .tiff RGB files using FIJI. The image files were then binarized, skeletonized, and traced using a custom MATLAB script. The traced images were converted to .DXF files using the DXFLib package (Kwiatek, 2023) and imported into AutoCAD to overlay the schematics for the microfluidic devices. The traced vessels and microfluidic devices were imported into COMSOL 5.2.1. The velocity and shear stress were calculated using the laminar flow steady-state model, with water as the fluid material. Using the Bernoulli equation, all pressure heads were calculated based on medium height in the inlet/outlet wells to provide input to the COMSOL model.

Plotting and Statistical Analysis

All plots were generated in RStudio (Allaire, 2012) using R version 4.0.3 with the ggplot2 package (Wickham, 2011), ggpubr package (Kassambara, 2020), grid package (Murrell, 2002), and gridExtra package (Auguie, 2017).

For ELISAs and qPCR data, one-way ANOVAs with post-hoc Tukey's HSD tests were run using the rstatix package (Kassambara, 2020) for parametric data. For nonparametric data, a Kruskal-Wallis H test was run with a Conover-Iman post hoc test using the conover.test package (Dinno, 2017). For the time course for MFI infectivity at various doses Fig 2F, an unbalanced two-way ANOVA on rank-transformed data was run using the car package (Fox, 2012), and the type III sum of squares was used to determine the significance of the main effects and interactions. Tukey's HSD was run to determine significance between treatments.

Results

A Microphysiological Model for Vascular SARS-CoV-2 Infection

The VMO is a 3D vascularized microtissue platform comprising endothelial cells (ECs), and stromal cells (fibroblasts, pericytes, etc.), suspended in an extracellular matrix (ECM) that we have used as a base platform for the development of multiple tissue-specific models including heart, pancreas, liver, brain and tumors. Here we have used a modified version of this device to study infection of the vasculature by the COVID-19-causative agent, SARS-CoV-2. We array 16 individual tissues in a 96-well plate format, where each unit consists of three interconnected tissue chambers that rely on hydrostatic pressure to drive interstitial flow through the vessels (Fig. 1A). Once seeded as a dispersed cell suspension in gel the ECs and fibroblasts undergo vasculogenesis and angiogenesis over the course of 4-5 days to form a perfusable vascular network (Moya, 2013). ECs also migrate into the microfluidic channels that represent the artery and vein, and these anastomose with the vascular network to allow for pressure-driven fluid flow from the artery, through the network and out of the vein. In this study, the microfluidic channels were increased from 100 to 200 microns on each side to assist endothelial attachment to the walls of the outer channels. The perfused vasculature thereby experienced physiologically-relevant fluid flow and shear stress (Roux, 2020) (Fig. 1B, C).

Vasculature in the VMO is a Target for SARS-CoV-2 Infection

A non-replicative pseudotyped virus was generated consisting of HIV-1 Gag fused to GFP and enveloped with original strain SARS-CoV-2 spike protein. The spike protein of COVID-19 recognizes the cell surface receptor ACE2 and is reliant on binding to it to enable membrane fusion (Li, 2003), with TMPRSS2 acting to prime the spike protein (Hoffman, 2020). Downstream of ACE and ACE2 is AGTR1/AT1R, which responds to angiotensin II to activate the classical, proinflammatory arm of the renin-angiotensin system (Kouhpayeh, 2021). We first

compared the RNA expression levels of ACE2, TMPRSS2, and AGTR1 in endothelial monolayers, and in the VMO at both day 4 and day 8 (Fig. 2A-C). We observed a significant increase in ACE2 and AGTR1 expression in the VMO vasculature compared to cells in monolayer, and expression was higher once flow was fully established (day 8) compared to the early stages of lumen formation (day 4). There was no apparent change in TMPRSS2 mRNA expression in the VMO. We performed immunofluorescence staining and confirmed ACE2 and TMPRSS2 in the VMO (Fig. 2D). Consistent with our expression data showing an extremely low level of ACE2 expression by monolayer EC, these cells were not infectable with pseudotyped virus; however, they were infectable with a control GFP-expressing virus (Fig. 2E). In contrast, the pseudovirus readily infected the endothelium when perfused through the VMO for 48 hours (Fig. 2F, G), again consistent with our expression data showing induction of ACE2 under flow conditions. We hypothesized that the increase in ACE2 in the VMO is likely caused by exposure to shear stress, as shown by others (Song, 2020). To test this directly we exposed monolayer ECs to a range of shear stresses, comparable to those found at various points throughout the vascular network in the VMO. Analysis of mRNA expression revealed that ACE2 is indeed induced dose-dependently by flow (Fig. 2H).

SARS-CoV-2-Pseudotyped Virus Infection in the VMO Generates Local EC Inflammation

Having demonstrated that EC in the VMO are infectable by a SARS-CoV-2-pseudotyped virus we next wished to determine how the concomitant loss of ACE2 would affect EC phenotype. In the body, the effects of angiotensin (AngII), mediated by AGTR1, are transient due to the rapid degradation of AngII by ACE2. Peptide degradation products of this reaction (specifically Ang_{1-7}) then bind to the Mas receptor (MasR), which mediates an anti-inflammatory signal. Loss of ACE2 leads to prolonged activation of AGTR1 and loss of MasR signaling, which has been shown to be pro-inflammatory (Mahmudpour, 2020). We therefore tested whether recombinant AngII (rAngII) in the presence or absence of pseudotyped virus would reduce

ACE2 expression, and whether this would lead to a proinflammatory EC phenotype in the VMO. Consistent with our hypothesis, both rAngII and the pseudotyped virus reduced ACE2 expression on EC in the VMO (Fig. 3A, B). AGTR1 expression was also reduced. Somewhat surprisingly we also saw a decrease in expression at the mRNA level at 48 hours (Fig. 3A, B), however such a loss has been previously reported (Gutierrez-Chamorro, 2021).

We then evaluated expression of two key leukocyte adhesion molecules expressed by EC – ICAM-1 and VCAM-1, which are typically upregulated on EC in response to inflammatory stimuli such as IL-1 and TNF (Bui, 2020; Kong, 2018), but also by the pleiotropic proinflammatory cytokine IL-6, the elevated expression of which is often associated with cytokine storms (Kang, 2021). We found both genes to be strongly upregulated by a combination of pseudotyped virus and rAngII (Fig. 3E-F). Interestingly, ICAM-1 was also upregulated by either challenge alone, whereas VCAM-1 was induced by pseudotyped virus but not by rAngII alone. IL-6 followed the pattern of ICAM-1 being induced by virus or rAngII alone, or in combination (Fig. 3G). Thus, our data suggest that loss of ACE2 as a consequence of viral infection in COVID-19 can lead to the expression of pro-inflammatory genes by the vasculature.

To better understand how this proinflammatory signature might disrupt the local vascular niche, we quantified morphological changes in the vasculature induced by the modeled COVID-19 infection (Fig. 4A). Subsequent to infection we noted a modest reduction in total vessel length (Fig. 4B), vessel diameter (Fig. 4C), and an increase in lacunarity (Fig. 4D), which characterizes vessel non-uniformity and is often increased in pathological vasculature (Zudaire, 2011). In addition, although not significant, there was a trend towards a reduction in vessel percentage coverage (Fig. 3E); however, there was no change in the total number of endpoints (Fig. 3F), suggesting that angiogenic sprouting was not induced.

SARS-CoV-2-Pseudotyped Virus Infection in the VMO Stimulates Release of Soluble Inflammatory Mediators

We wished to characterize the extent to which a localized COVID-19 infection could generate downstream inflammation. To better understand the proinflammatory and pro-thrombotic environment produced by infected ECs (Xu, 2010), we investigated inflammatory protein secretion via ELISA (Fig. 5). Coagulation Factor VIII is secreted from Weibel-Palade bodies by EC and is a cofactor for activating factor IX, which induces the coagulation cascade (Turner, 2015). In perfused VMOs treated with rAngII, pseudotyped virus, or a combination of the two, there was an increase in coagulation Factor VIII secretion (Fig. 5A). Additionally, there was increased secretion of several EC-derived inflammatory molecules previously identified in COVID-19 patients (Xu, 2023), including IL-1β, IL-6, and sICAM-1 (Fig 5B-D). To determine whether the combination of factors released by infected EC might have effects on distant vessels – i.e. systemic effects – we collected effluent from the treated tissues and added this to EC transduced with an NFκB promoter-mCherry reporter. NFκB is a key pro-inflammatory transcription factor in EC. As shown in Fig. 6B, we found a strong induction of mCherry by supernatant from VMOs previously treated with virus and rAngII (and subsequently fed with fresh medium in the absence of virus or recombinant protein) that was apparent by 24 hours of treatment. Interestingly, medium from VMOs treated with pseudotyped virus alone had no effect, while medium from rAngII-treated VMOs had a slower effect than the combination. These data are therefore consistent with a mechanism whereby local infection of EC by SARS-CoV-2 could lead to systemic effects due to released cytokines and pro-coagulatory factors.

Pharmacological Intervention Blocks SARS-CoV-2-Pseudotyped Virus Infection

A potential application for the VMO is the ability to conduct drug studies (Phan, 2017), and so we tested the efficacy of camostat mesylate – a TMPRSS2 inhibitor (Hoffman 2020) –

and recombinant ACE2. As shown in Fig. 6A, rACE2 almost completely blocked infectivity by the pseudotyped virus, whereas TMPRSS2 had only a moderate impact on infectivity.

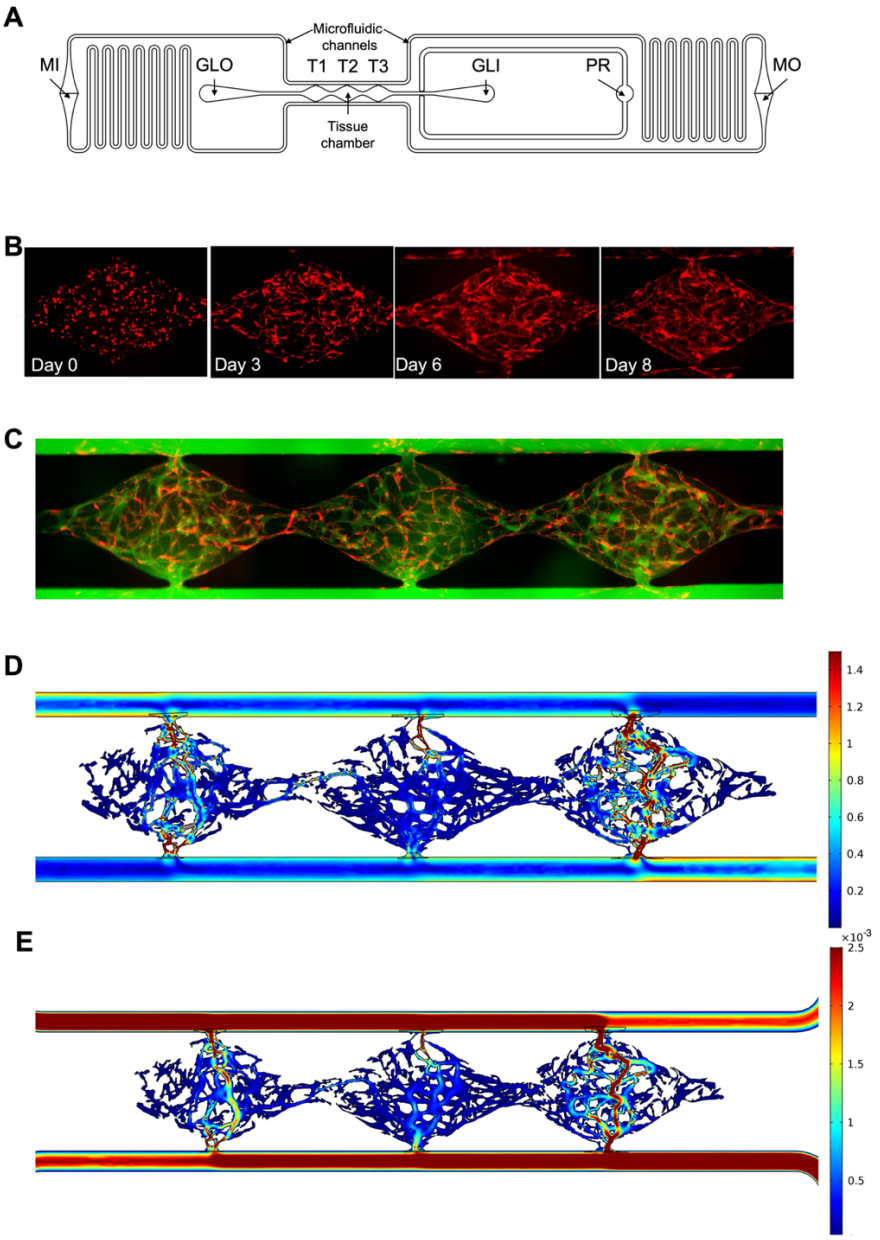

Figure 1. Development of a vascularized micro-organ microphysiological system and SARS-CoV-2 pseudotyped virus. A) schematic of an individual microfluidic device unit. Hydrostatic pressure drives medium from the inlet (MI) through the microfluidic channels and tissue chamber (T1-T3) to the medium outlet (MO). Hydrogel is loaded via the gel loading inlet (GLI) and outlet (GLO) with the pressure regulator (PR) to prevent leak into the microfluidic channel. B) Development of the vasculature over time. Endothelial cells labeled red; fibroblasts unlabeled. C) Perfusion of 70kDa FITC-Dextran through the vasculature (endothelial cells eRFP) at day 8. D) COMSOL modeling of the shear stress (dynes/cm^2) through each of the tissue chambers. E) Quantification of shear stress along the main path of flow in each tissue chamber.

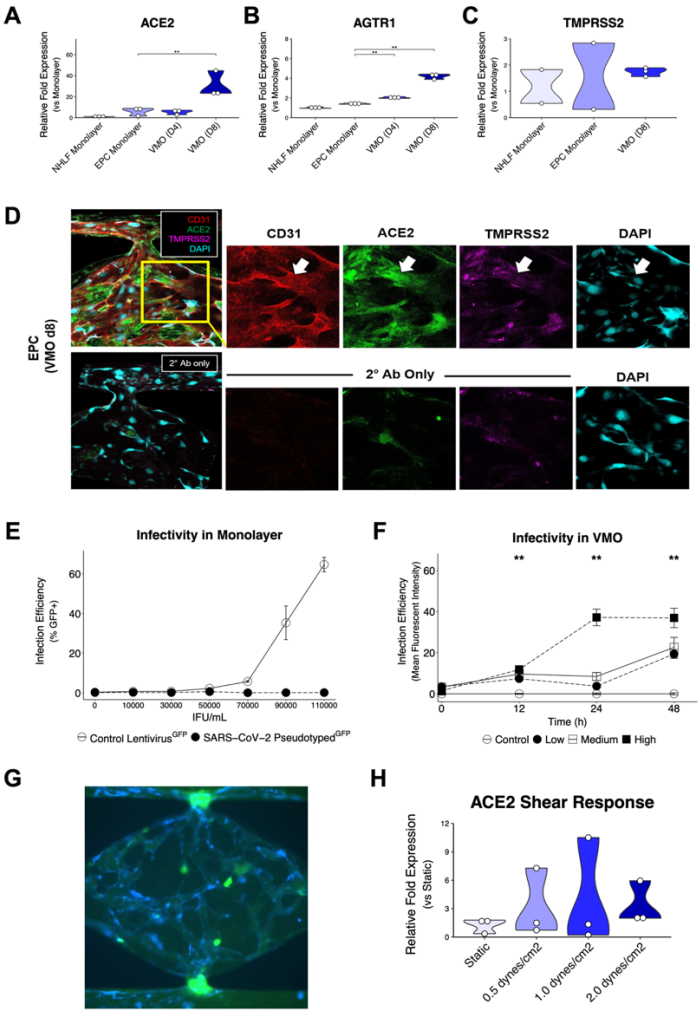

Figure 2. Upregulated ACE2 expression in the vascularized micro-organ supports SARS-CoV-2 pseudotyped infectivity. qPCR analysis of (A) ACE2, (B) AGTR1, and (C) TMPRSS2, which are necessary for SARS-CoV-2 infectivity, comparing monolayer normal human lung fibroblasts (NHLF), monolayer endothelial progenitor cells (EPC), the vascularized micro-organ (VMO) before (D4) and after (D8) the formation of perfusable vasculature. * < 0.05, ** < 0.01. (D) Immunofluorescence staining of a D8 VMO showing CD31/PECAM1 (red), DAPI (blue) and localization of ACE2 (green) and TMPRSS2 (purple) to the endothelium. Showing nonspecificity of secondary antibodies alone. (E) Infectivity efficiency (mean fluorescent intensity) of SARS-CoV-2 pseudotyped virus compared to a lentivirus expressing green fluorescent protein (GFP). (F) Titering of GFP SARS-CoV-2 pseudotyped virus in a perfused VMO. Infectivity measured as increase in mean fluorescent intensity of GFP channel. * = p-value <0.05 vs control, ** = p-value <0.01 vs control. (G) Subset of a D8 VMO infected with SARS-CoV-2 pseudotyped virus (GFP) of endothelial cells (eBFP). (H) qPCR analysis of ACE2 expression induced by shear stress in an ibidi microfluidic chip.

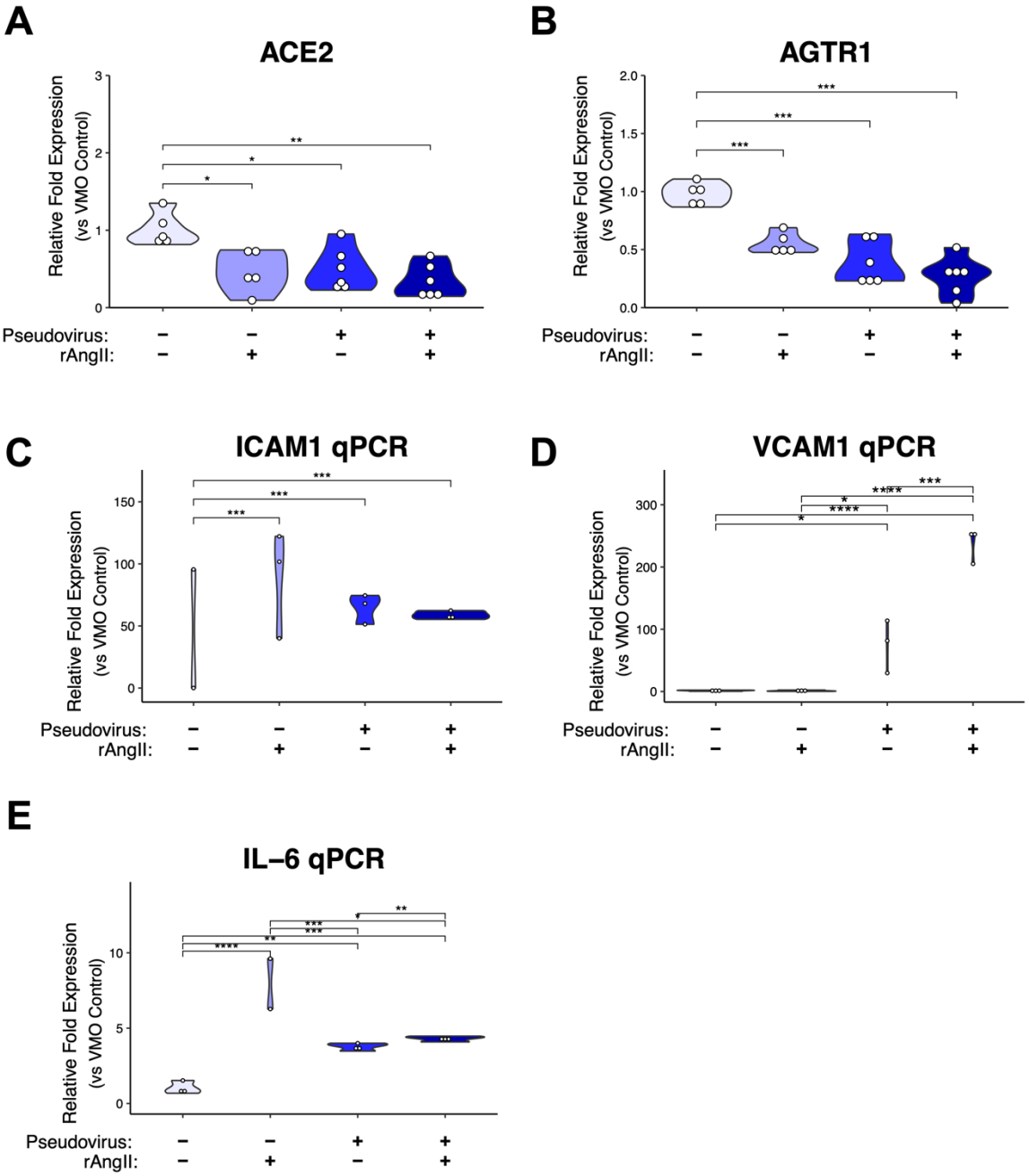

Figure 3. Modeled SARS-CoV-2 infection alters vascularized micro-organ transcriptomic profiles. qPCR analysis of (A) ACE2 and (B) AGTR1, for perfused vascularized micro-organ (VMO) that have been treated with SARS-CoV-2 pseudotyped virus (pseudovirus), recombinant angiotensin II (rAngII) or both for 48 hours. (C-E) qPCR analysis of pro-inflammatory markers, (C) ICAM-1, (D) VCAM-1, and (E) IL-6 from perfused devices treated with rAngII or pseudovirus for 48 hours. * < 0.05, ** < 0.01, *** < 0.001.

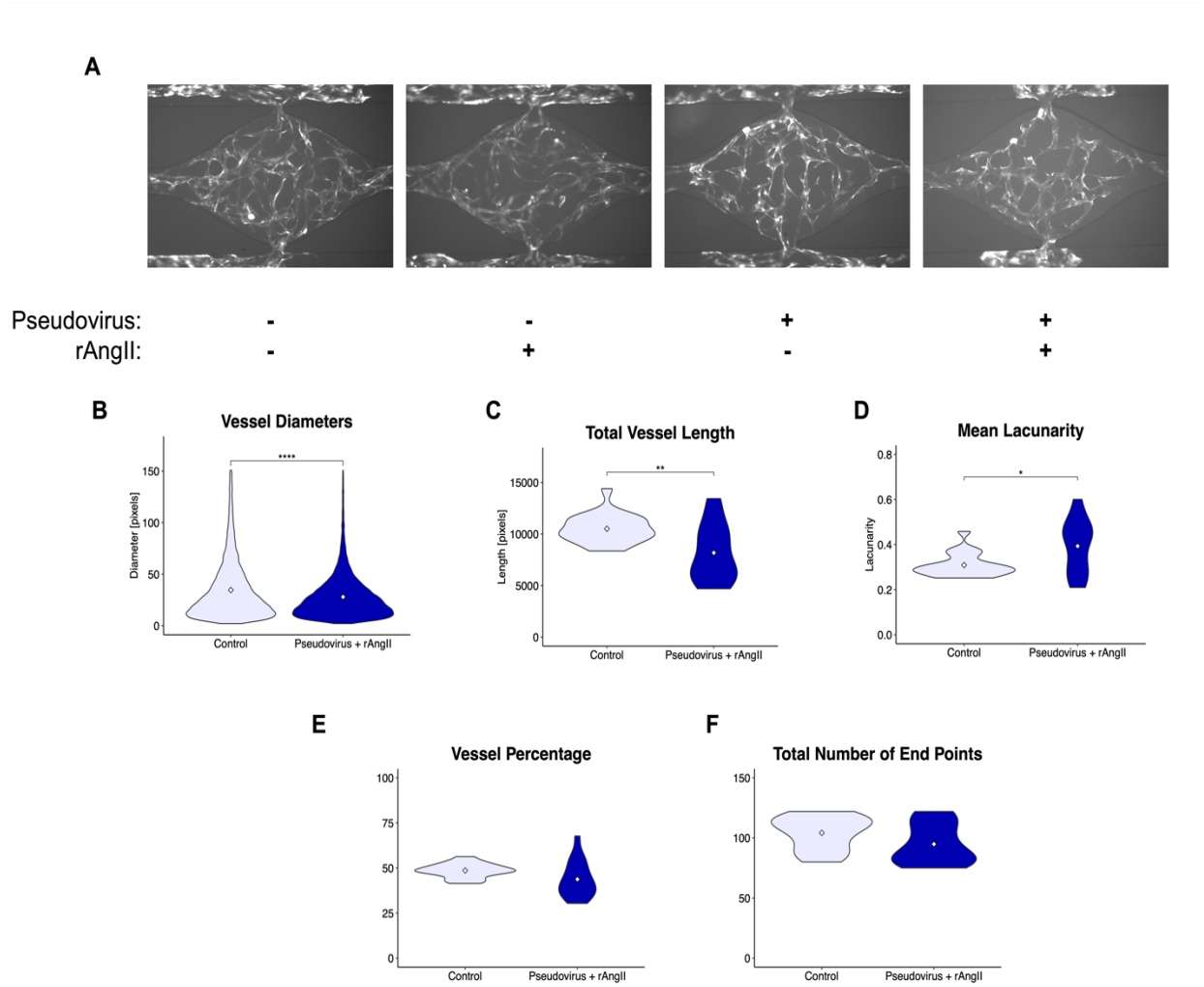

Figure 4. Modeled SARS-CoV-2 infection alters vascularized micro-organ morphometry. (A) Representative images of perfused vascularized micro-organs (VMO) that have been treated with SARS-CoV-2 pseudotyped virus (pseudovirus) and/or recombinant angiotensin II (rAngII) for 48 hours. (B-G) Quantification of morphometry of devices looking at changes in (B) vessel diameter, (C) total vessel length, (D) total number of end points, (E) mean lacunarity, and (F) vessel percentage. * < 0.05, ** < 0.01, *** < 0.001, **** < 0.0001.

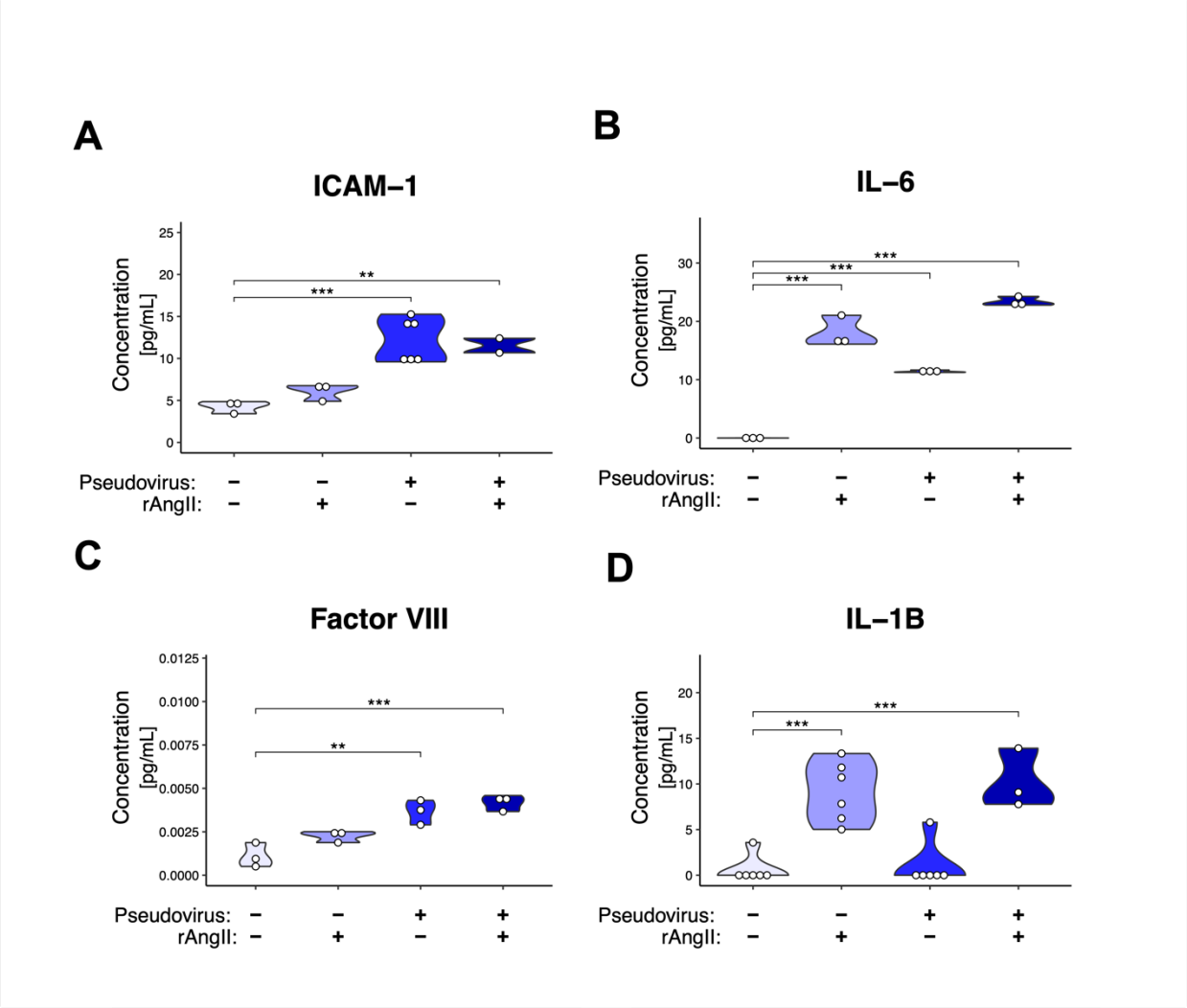

Figure 5. Modeled SARS-CoV-2 infection induces cytokine production. ELISAs from effluent collected from perfusable vascularized micro-organs that were treated with SARS-CoV-2 pseudotyped virus (pseudovirus) and/or recombinant angiotensin II (rAngII) for 48 hours. (A) ICAM-1, (B) IL-6, (C) Factor VIII, (D) IL-1B protein content (pg/mL). * < 0.05, ** < 0.01, *** < 0.001.

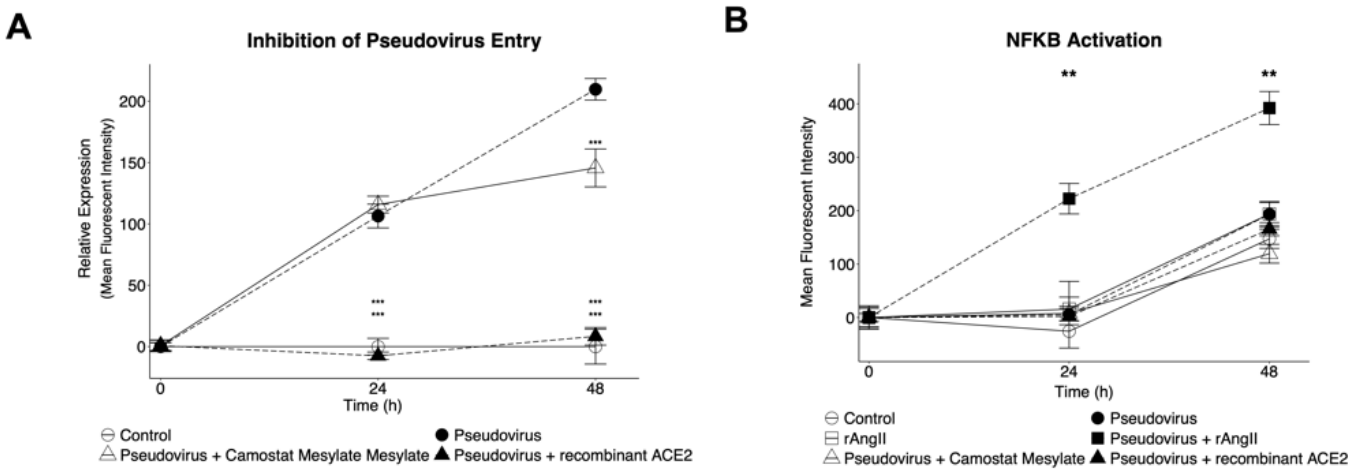

Figure 6. Pharmacological intervention inhibits SARS-CoV-2 pseudotyped virus entry and reduces downstream NFκB activation. (A) Perfusable vascularized micro-organs were treated with SARS-CoV-2 pseudotyped virus and recombinant ACE2 (rACE2) and camostat mesylate (camostat). The mean fluorescent intensity of the GFP pseudotyped virus was measured. (B) Effluent from non-treated and treated devices were placed on endothelial progenitor cells with a NFκB induced mCherry construct. The mean fluorescent intensity of mCherry was measured. * < 0.05, ** < 0.01, *** < 0.001, **** < 0.0001.

Discussion

Leveraging the unique benefits that the VMO provides, namely physiologically relevant flow rates and shear stress in a 3D environment comprised of human derived cells, allowed for real time analysis of COVID-19 infection and subsequent inflammatory response. Real time fluorescent imaging allowed for direct quantification of the rate of viral entry and propagation within the endothelium, demonstrating the pivotal role of ACE2 in viral infection under shear conditions.

While previous work has relied on animal models or static monolayer studies to provide insight into the mechanisms that drive hypercytokinemia and tissue damage (Droebner, 2008; De Jong 2006), we show in this work the importance of flow in studying the entry and clearance of ACE2 from the surface of endothelial cells. We hypothesized that the clearance of ACE2 from vasculature would result in a pronounced inflammatory response when challenged with physiological levels of angiotensin II and were able to demonstrate that the synergistic effect of viral exposure and angiotensin II was sufficient to significantly increase the inflammatory response in our microphysiological system.

Using the VMO allowed us to quantify this inflammatory response with a variety of metrics including immediate tissue damage in the form of vessel morphometry differences, cytokine production via proteomics and RT-qPCR, and downstream effects of effluent from the system on a secondary tissue with an NFκB reporter. While COVID-19 mortality rates are far lower since the introduction of mRNA vaccines (Mohammed, 2022), there is still a pressing need to better understand both the acute infection stage as well as the long-term effects of the disease following recovery. Currently it is theorized that the profound impact of long-term COVID is due to dysregulation of thrombotic pathways leading to disseminated intravascular coagulation (Asakura, 2021; Crook, 2021). The VMO, along with other microphysiological systems, provides a unique avenue to study thrombosis and coagulation in a real time system.

Additionally, we have demonstrated that these microphysiological systems enable us to study the impact of potential therapeutics such as rACE2 and camostat mesylate on reducing viral entry. The efficacy of these two candidate drugs was demonstrated by the inhibition of viral entry; the prospect of using an organ-on-a-chip system to screen for further treatments is enticing given the immense impact COVID-19 has had on a global scale.

Conclusion

We used our VMO platform to demonstrate both the role of flow on COVID-19 infection in a vascular model as well as showing the deleterious effects of ACE2 clearance from the lumen of the vasculature on hyperinflammation. Additionally, we have begun to glean insights into how thrombotic dysregulation can arise during an active COVID-19 infection and how that might impact the ultimate disease outcome. Given rapid globalization and human expansion it is highly likely that more zoonotic viruses similar to SARS-CoV-2 will arise in the coming decades. Microphysiological systems such as the VMO will allow us to adopt rapid responses to both new strains of SARS-CoV-2 as well as whatever unknown viruses are yet to emerge.

Chapter 2:
Development and application of a novel single channel arteriole microphysiological system for characterizing leukocyte-endothelial interactions

Abstract

In this chapter, I present a novel approach to evaluate peripheral blood mononuclear cells using a microfluidic model designed to approximate the complexity of a human arteriole. This model is comprised of a hydrogel suspension of stromal cells that supports an inner lumen of endothelial cells with a diameter in the range of a small arteriole. Given appropriate shear conditions this three-dimensional organoid on a chip developed distinct differences from the widely applied human umbilical vein endothelial cell (EC) monolayer model. While EC monolayer assays are commonly used to investigate leukocyte-endothelial cell interactions, we hypothesized that our arteriole on a chip would recapitulate the microvasculature more accurately and provide additional insight into the initial stages of atherogenesis. Significant differences were found between the SCA and monolayer cultures in the expression of key EC and stromal cell markers, including ICAM-1, VCAM-1, PDGFB, α-SMA, and KLF2. Indeed, flow-induced PDGFB expression likely mediated the recruitment and differentiation of α-SMA-positive cells to the vessel wall. Importantly, the vessels were responsive to stimulation by inflammatory mediators, showing both increased leukocyte adhesion and increased permeability. Finally, mechanically-mediated protrusion of the vessel wall into the lumen disrupted flow, producing increased shear over the vessel wall. Our studies characterize an exciting new model that could be further developed into a model of atherosclerosis with the addition of macrophages and high lipid levels. In addition, our data emphasize the advantages of complex 3D assays over more traditional 2D cultures.

Introduction

One of the most pressing public health concerns in the United States is the high prevalence of cardiovascular disease (CVD) (Mensah, 2007). CVD is the leading cause of death in the United States, and with over 12% of the population diagnosed it is also one of the greatest disease burdens on our society (Gunby, 1992; Barret-Connor, 2011). The costs imposed on hospital systems by CVD is massive (Kahn, 2008) and the loss of quality of life in patients unquantifiable. While the late stages of CVD can be measured in a variety of metrics (Ledue & Rifai, 2003; D'Agostino, 2013; Stein, 2008), the pathogenesis of atherosclerosis is relatively poorly understood (Ross, 1986). The primary stage of disease development is initiated by a dysregulation of leukocyte-endothelial interactions during childhood and adolescence (Strong, 1969; Kannel, 1972). These incidences eventually accrue and form fatty streaks, followed by true plaques (Libby, 2000). This early stage of CVD in humans is currently impossible to investigate, precluding autopsy studies (Roberts, 1959).

What is currently known is that in the United States the presence of fatty streaks is found in most of the childhood and young adult autopsies (Fausto, 1998). Naïve endothelium can be stimulated via exogenous or endogenous pathways to either reduce or overexpress key leukocyte adhesion molecules, including ICAM-1 and VCAM-1 (Lawson & Wolf, 2009; Munro, 1993). For example, physical activity and certain dietary measures result in a decrease in gross plaque formation while smoking and high-glucose exposure will result in accelerated plaque growth (Palmefors, 2014; Bertoni, 2009; Rafieian-Kopaei, 2014). Previous research from the UCI Pediatric Exercise Research Center has demonstrated that even brief bouts of exercise induce shifts in gene expression in circulating immune cells, providing insight into the molecular pathways that may drive monocytes towards either a pro- or anti-inflammatory phenotype (Radom-Aizik, 2010; Radom-Aizik, 2012). While we can follow late-stage atherosclerotic plaque

formation in patients via ultrasound imaging, the initial kinetics of leukocyte-endothelial interactions are more difficult to visualize and challenging to accurately measure. To comprehend the full scope of the pathogenesis it is critical to quantify these cell-to-cell interactions and investigate the molecular markers associated with adhesion and extravasation.

The standard method of observing leukocyte-endothelial dynamics in vitro is monolayer endothelial cell culture plates (Muller, 2003). While these studies do provide insight into the adhesion of leukocytes to vascular surfaces, there are certain shortcomings. Endothelial monolayer studies typically lack shear flow, which is critical in the pathogenesis of atherosclerosis given leukocytes' lack of innate motility (Alon & Ley, 2008). Additionally, monolayer models are lacking in three-dimensional complexity, leading to significant differences in endothelial gene expression and function (Buchanan, 2014). Atherosclerosis primarily occurs in high shear, relatively large arteries downstream from turbulent bifurcation points (Gijsen, 2013). Rather than rely on solely monolayer measurements, we present here a novel three-dimensional single channel arteriole model to replicate the hallmarks of atherosclerotic arteries.

The SCA provides a more accurate representation of the high-risk arteries for atherosclerosis development than standard monolayer culture. The pump system utilized allows for a high shear flow to be passed across multiple channels immediately downstream from the pump source. These channels are composed of human endothelial cells overlaying a stromal cell-rich matrix, closely modeling the complex composition of naturally occurring tissues (Phan, 2017). This vascular tissue on a chip can be kept in culture for a comparable period as monolayer plates and imaged via fluorescent microscopy, allowing for long term visualization of the adhesion and extravasation of leukocytes across the endothelial barrier.

Using this novel platform, we have been able to quantify the initial stages of atherogenesis with high-fidelity. While long-term health patterns in clinical populations are challenging to replicate in cell culture, the SCA presents significant differences from monolayer endothelial cells in key mediators of leukocyte transmigration, namely ICAM-1 and VCAM-1 as

measured by qPCR creating an improved and nuanced endothelial model. We noted recruitment of stromal cells to the EC layer and induction in these cells of smooth muscle alpha actin (αSMA). Over time we found strong induction of shear-responsive genes and saw a robust response of the EC to treatment with TNFα, resulting in increased adherence of PBMC flowed through the vessels. Additionally, we modified the geometry of the SCA by introducing occlusions along the length of the vessel that mimicked the protrusion of plaques into the vessel lumen, thus allowing for study of altered flow dynamics (Insull Jr, 2009).

Methods

SCA Platform Design and Fabrication

Using a laser cut acrylic mold the base of the chip is principally based on a two-part polyurethane liquid plastic that acts as a master mold for subsequent polydimethylsiloxane (PDMS) replicas. The base layer of the chip is fabricated from PDMS, which following an overnight curing has inlet and outlet holes punched prior to being mounted onto a 50 mm-60 mm, .5 mm thickness glass slide. The slide and PDMS chip are bonded by exposure to oxygen plasma for three minutes and again allowed to set overnight in a 60°C oven. The bonded chip then has male 1/16" bore luer lock valves (McMaster-Carr, 75165A675) inserted and affixed into place using PDMS at either end of the tissue chamber. Following the insertion of the luer lock inlets a .8 mm diameter nitinol wire (McMaster-Carr, 8320K34) is inserted through the apertures to bridge the tissue chamber and provide the space that will eventually form the lumen of the arteriole (Fig. 1A-C). This final assembly is then sterilized by exposure to UV light for 30 minutes and is viable for use for up to 4 months.

Cell Culture

There were two primary cell types used in the experiments described. Human umbilical vein endothelial cells (HUVEC, referred to as EC) that were isolated from fresh cord tissue acquired through the UCI Douglas Hospital with internal approval (Crampton, 2007). It is important to note that although HUVEC occupy a vein position – carrying blood toward the (fetal) heart – they are actually carrying oxygenated blood from the placenta, and thus have some arterial characteristics. EC were cultured on gelatin coated cell culture flasks in EGM-2 (Lonza, CC-3162) medium. Normal human lung fibroblasts (NHLF, Lonza) were cultured in DMEM (Corning, 10027CV) with 5% FBS (VWR, S1700-100). Both HUVEC and NHLF were transduced with lentiviruses encoding fluorescent proteins (mCherry/Addgene, 36084 or Azurite/Addgene, 36086) and were used between passages 5-9. All cells were cultured at 37° C/20% O_2/5% CO_2 in incubators with cupric sulfate baths in the base.

SCA Platform Loading

Immediately following UV exposure the chip was ready for loading. A solution of fibrinogen (Sigma-Aldrich, 9001-32-5) was prepared at 12 mg/mL in EGM-2 and kept at room temperature while the NHLF were lifted from their flasks and suspended in the gel-cell mix at a concentration of 2 million cells/mL. This solution was rapidly mixed with thrombin and pushed through the negative space within the chamber of the chip. This was repeated in quick succession through the next three devices on the chip before the device were placed in an incubator for 30 minutes to allow for gel polymerization. Following polymerization the nitinol wires were removed from the matrix, leaving a vacant channel. Each channel was then flushed with laminin (0.5 mg/mL, Life Technologies) to support the adhesion of EC and provide the basis of a basement membrane. The EC suspension was prepared in EGM-2 at a concentration of 4 million cells/mL and perfused through the lumen prior to being capped at either end and

allowed to rest for an hour. This allows for the EC to settle and anchor on the matrix. After an hour the devices were flipped to ensure even distribution of the cells.

Platform Flow Metrics

Following an overnight culture post-loading the devices were hooked together in series or in parallel using 1/16" polyurethane microfluidic tubing (Cole- Parmer, EW-21942-76) segments. Once assembled a syringe pump (New Era Syringe Pump Systems Inc.) was hooked onto the top of the chip and set to flow at a rate of 2 mL/hour, slowly pushing the EC that did not attach to the matrix to be removed from the lumen of the devices. After five hours of this flushing the flow rate across the arterioles was increased to a rate of 5 mL/hour for 24 hours. During this period the gel continued to set as the NHLF remodeled and deposited additional ECM in the fibrin gel, allowing for the devices to accommodate higher flow. After 24 hours of flow the media was replaced with a blood substitute media consisting of of EGM-2 mixed with xantham gum (Sigma, 11138-66-2) to achieve a viscosity of 3.5 cP. This viscous blood substitute is then placed into the reservoirs of the New Era Syringe pump system and the flow was set to 25 mL/hour for 48 hours. Following this 48-hour period of flow with the blood substitute, the flow rate was set to 50 mL/hour to achieve a shear stress of 10 dyne/cm^2 across the arteriole wall. This rate can be maintained for up to several days with the devices remaining functional. For all experiments requiring an inflammatory stimulus, The SCA devices or monolayer culture were perfused with TNF-α (Sigma, 11088939001) at a concentration of 9 ng/mL for 24 hours.

Peripheral Blood Mononuclear Cell (PBMC) Perfusion

The PBMCs were isolated from donated blood provided by the UCI ICTS blood donor system using Ficoll gel gradient CPT tube (BD Biosciences, 362753). These isolated PBMCs were then rinsed and brought to a concentration of 1.5 million cells/mL before being stained with CellTracker Green dye (Thermo-Fisher, C2925) according to the manufacturer's instructions.

Post-staining the PBMCs were assessed for viability with trypan blue, counted, and rinsed. Following perfusion at a shear stress of 10 dyne/cm^2 for 24 hours the devices were removed from the incubator and fresh blood replacement media with CellTracker-labelled PBMCs at a concentration of 250,000 cells/mL were added. This cell suspension was then perfused across the single channel arteriole chip for 24 hours and imaged at the 6-, 12-, and 24- hour timepoints. Prior to imaging the devices as well as the monolayer comparisons were gently washed with media to remove any non-adherent cells from the system.

Imaging

At the 6-, 12-, and 24-hour time point the channels were imaged along the entirety of the arteriole length using a Nikon Ti-E Eclipse epifluorescent microscope with a 4xPlan Apochromat Lambda objective. These images were then analyzed using FIJI (Schindelin, 2012) and adherent and extravasated labelled PBMCs were enumerated. Once cell counts had been established final leukocyte adhesion was normalized to endothelial surface area of the channel.

RNA isolation and qRT-PCR analysis

In order to extract RNA from the tissue chamber the glass cover slip was gently pared off of the PDMS mold and both the surface of the slip and the tissue chamber are treated with 200 uL of Trizol and the resulting cell lysis volume was collected and prepped using a Quick RNA micro prep kit (Zymo Research, R1051) according to manufacturer's instructions. Once the RNA isolation was complete a cDNA library was prepared using Zymo-Seq Universal cDNA kit (Zymo Research, R3001) and qRT-PCR was performed for the gene targets in triplicate. The housekeeping gene selected to compare the gene targets was 18s ribosomal RNA. Monolayer HUVEC and SCA samples were standardized against monolayer HUVEC as well as CD31 expression. Primer sequences were designed and ordered via PrimerQuest Tool and synthesized using IDT technologies.

SCA Permeability Assay

Once the SCA was fully developed by day 4, a 70 kDa FITC-dextran (Sigma-Aldrich, D1823) was diluted in blood substitute media and flowed through the devices at a rate of 10 mL/hour. Images were taken at 5-minute intervals and mean fluorescence intensity was quantified in a demarcated region immediately adjacent to the lumen wall. Control devices were developed under standard blood substitute media conditions and then TNF-α was added at 9 ng/mL for 24 hours prior to the permeability assay.

Impingement of SCA

Prior to the fabrication of the platform, 1.5 mm biopsy punches were placed on opposite sides of the channel. Following the loading of the devices and development of the vessels over the course of four days, 1/8” diameter polypropylene spheres (McMaster-Carr, 1974K2) were injected into the biopsy punch space, displacing the outer wall of the PDMS channel into the stromal compartment (Fig. 5A). This displacement in turn created a consistent occlusion across the lumen of the arteriole of up to 50%, dependent on the placement of the biopsy punch during fabrication. Several of these occlusions can be placed along the length of a single arteriole, enabling complex flow dynamics to arise in an otherwise straight channel. These occlusions were stable fixtures along the length of the channel and remained in place for up to three days post introduction.

Computational Fluid Dynamics

Image masks were converted into .tiff RGB files using FIJI. The image files were then binarized, skeletonized, and traced using a custom MATLAB script. The traced images were converted to .DXF files using the DXFLib package (Kwiatek, 2023) and imported into AutoCAD to overlay the schematics for the SCA. The traced vessels and microfluidic devices were

imported into COMSOL 5.2.1. The velocity and shear stress were calculated using the laminar flow steady-state model, with blood as the fluid material. Using the Bernoulli equation, the pressure was calculated based on the steady flow rate driven by the linear syringe pump to provide input to the COMSOL model.

Plotting and Statistical Analysis

All plots were generated using Microsoft Excel and figures were generated using Bio Render. Statistical Analysis was performed using Microsoft Excel, for qPCR analysis was run using one-way ANOVA, and comparison between TNF-α and control SCA for both the permeability assay and PBMC adhesion was made using a two-tailed t test to determine significance at alpha less than 0.05.

Results

Establishment of the SCA

The tissue chamber housing the lumen of the SCA provides ample space for the extracellular matrix to undergo remodeling over the course of arteriole development. Once the gel containing the NHLF had set the wire was carefully removed and the resulting channel seeded with EC. These became confluent over the next 2-3 days. During this time the NHLF began to undergo distinct morphological changes (Fig. 1D). Notably, as the NHLF proliferated and remodeled the matrix the cells were drawn towards the basolateral side of the lumen of the SCA, where they wrapped the vessel in a manner reminiscent of pericytes and smooth muscle cells. Concomitantly, the shear tolerance threshold of the system increased as the vessel became capable of sustaining perfusion at significantly higher flow rates (Fig. 1D). EC were stripped from the walls and the gel collapsed if high flow rates were established immediately. Over the course of four days the shear tolerance increased from .5 dyne/cm^2 up to 10 dyne/cm^2.

This improvement in system resilience was critical in meeting the shear range that correlates with that found in small arterioles in the human body (Takeishi, 2014).

Gene Expression Differences Between Monolayer and SCA

Following four days of development, RNA was harvested from the tissue chamber and qPCR was performed. The EC monolayer cDNA libraries were generated from the same cell preparation used to load the SCA. We found significant differences in expression of ICAM-1, VCAM-1, PDGFB, α-SMA, and KLF2 (Fig 2A-E). These results are indicative of major shifts in both cell types present in the SCA in response to the onset and increase in shear. The recruitment of NHLF to the vessel wall correlated with an increase in α-SMA expression, indicative of fibroblast differentiation to smooth muscle cells (Fig. 2E). Notably, we also saw an increase in PDGFB expression in response to shear (Fig. 2D): PDGFB is the major signal for pericyte and SMC recruitment to vessel walls under flow conditions. An early response of EC to shear is the upregulation of KLF-2 and this was reproduced in the SCA system with expression being absent in monolayer and proportional to the shear level in the SCA (Fig. 2C). Finally, we saw little change in ICAM or VCAM expression under flow conditions, although both were lower than in monolayer (Fig. 2A-B).

Interestingly, the basal level of expression of ICAM-1 and VCAM-1 in EC under flow conditions appeared to be substantially higher than that seen in monolayer cultures (Fig. 2A-B). TNF treatment induced a strong induction of both ICAM-1 and VCAM-1 mRNA expression by monolayer EC, whereas induction in EC under flow was more modest.

PBMC Adhesion and Extravasation

Once the devices were mature, perfusion of PBMCs through the vessel was performed to evaluate the capability of the SCA to model leukocyte-endothelial transmigration, in comparison to monolayer cultures. Both the monolayer EC and SCA were confluent, and the

adhesion and extravasation of the PBMCs were standardized to the surface area of EC in each model (Fig. 3A). In both cases we observed a time-dependent increase in PBMC adhesion, and this was significantly increased by prior treatment of the cells with TNF (Fig. 3B). While the increase in PBMC adhesion in response to TNF treatment in the SCA was consistent with the upregulation of ICAM-1 and VCAM-1 expression (1.5 to 2-fold), this was not the case for monolayer where we found a similar fold increase in adhesion to that seen in the SCA in response, even though gene expression was induced several fold by TNF.

Permeability of SCA vessel in response to TNF-α

A key change that vessels undergo under inflammatory conditions is a weakening of junctional contacts leading to an increase in vessel wall permeability (ref). To test this we pre-treated vessels with TNF or control and then assessed permeability over time to 70kDa-FITC dextran, which models serum albumin (68kDa) in size. Over the course of 20 minutes there was a slow leak of FITC-dextran from the control vessels (Fig. 4), consistent with the usual bulk flow of fluid into peripheral tissues. This leak was significantly enhanced by pretreatment of the SCA with TNF-α (Fig. 4), again consistent with the known role of TNF-α in vascular inflammation.

Impingement of SCA and downstream flow perturbation

To accurately study the progression of atherosclerosis, which often occurs downstream of bifurcation points in areas of turbulent flow, we generated a proof-of-concept modification to the SCA model (Fig. 5B-E). A bead was inserted into a preformed hole in the gel adjacent to the vessel, which had the effect of reproducibly deforming the extracellular matrix such that the vessel wall impinged on the lumen (Fig. 5), in much the same way as an atherosclerotic plaque. These constrictions of the channel lead to a changes in the fluid flow pattern, as assessed by Comsol modeling. Specifically, we found an almost 5-fold increase in shear stress on the vessel

wall at the site of these artificial lesions. We did not detect turbulence, likely due to the too low Reynolds number at these flow velocities. We are currently examining ways to introduce a bifurcation or other flow-splitter that might generate turbulent flow. Nonetheless, the current model does demonstrate accelerated flow and shear over the surface of the artificial plaque, which could be used to model how shear may interact with damaged and inflamed endothelium, a forerunner to plaque rupture.

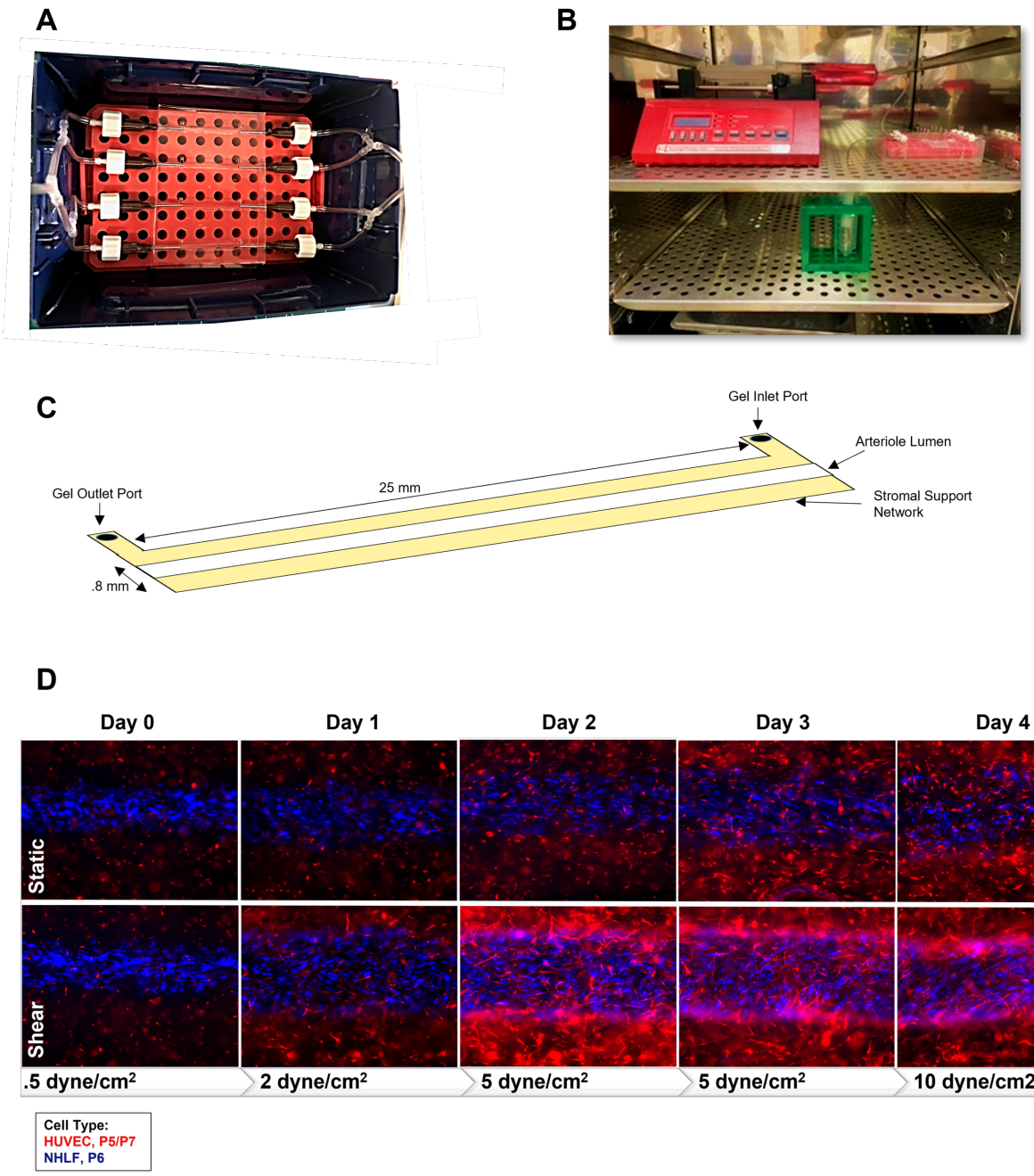

Figure 1. Single channel arteriole chip design and developmental timeline under static and shear conditions. (A) The SCA device arranged with media inlets and outlets in parallel. (B) Device connected to a linear syringe pump and media reservoir (below) in a tissue culture incubator. (C) Tissue chamber schema with relevant measurements. (D) SCA development over the course of four days under static and shear conditions.

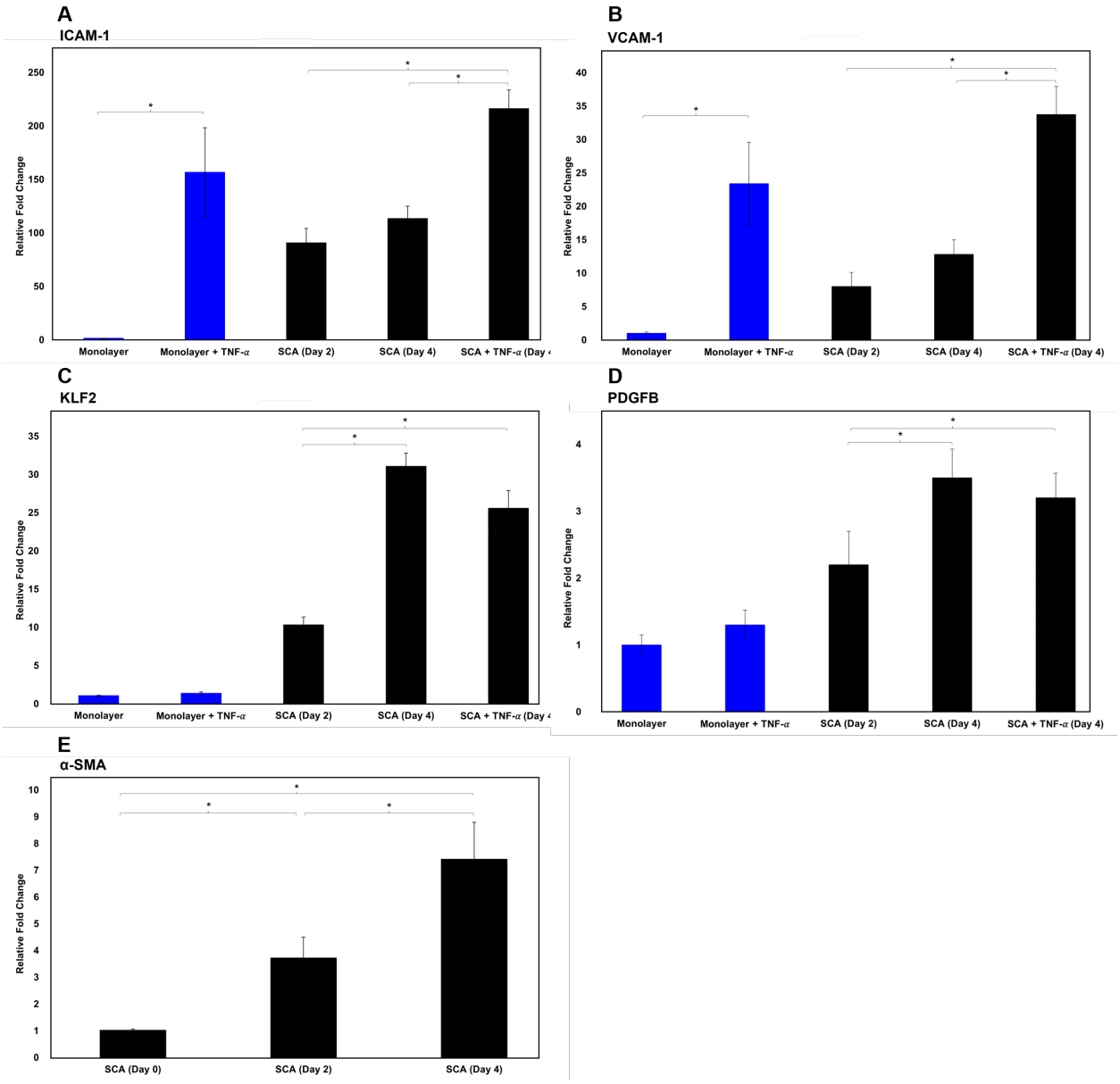

Figure 2. Gene expression analysis of inflammatory and developmental markers in SCA and EC monolayer. qPCR analysis of (A) ICAM-1 expression in both EC monolayer and SCA over time. Fold change normalized to HUVEC monolayer. (B) VCAM-1 expression in both EC monolayer and SCA over time. Fold change normalized to EC monolayer. (C) KLF2 expression in EC monolayer and SCA over time. Standardized to EC monolayer. (D) PDGFB expression in both EC monolayer and SCA over time. Fold change normalized to EC monolayer. (E) α-SMA expression in SCA over time. Fold change normalized to Day 0 SCA. *<0.05

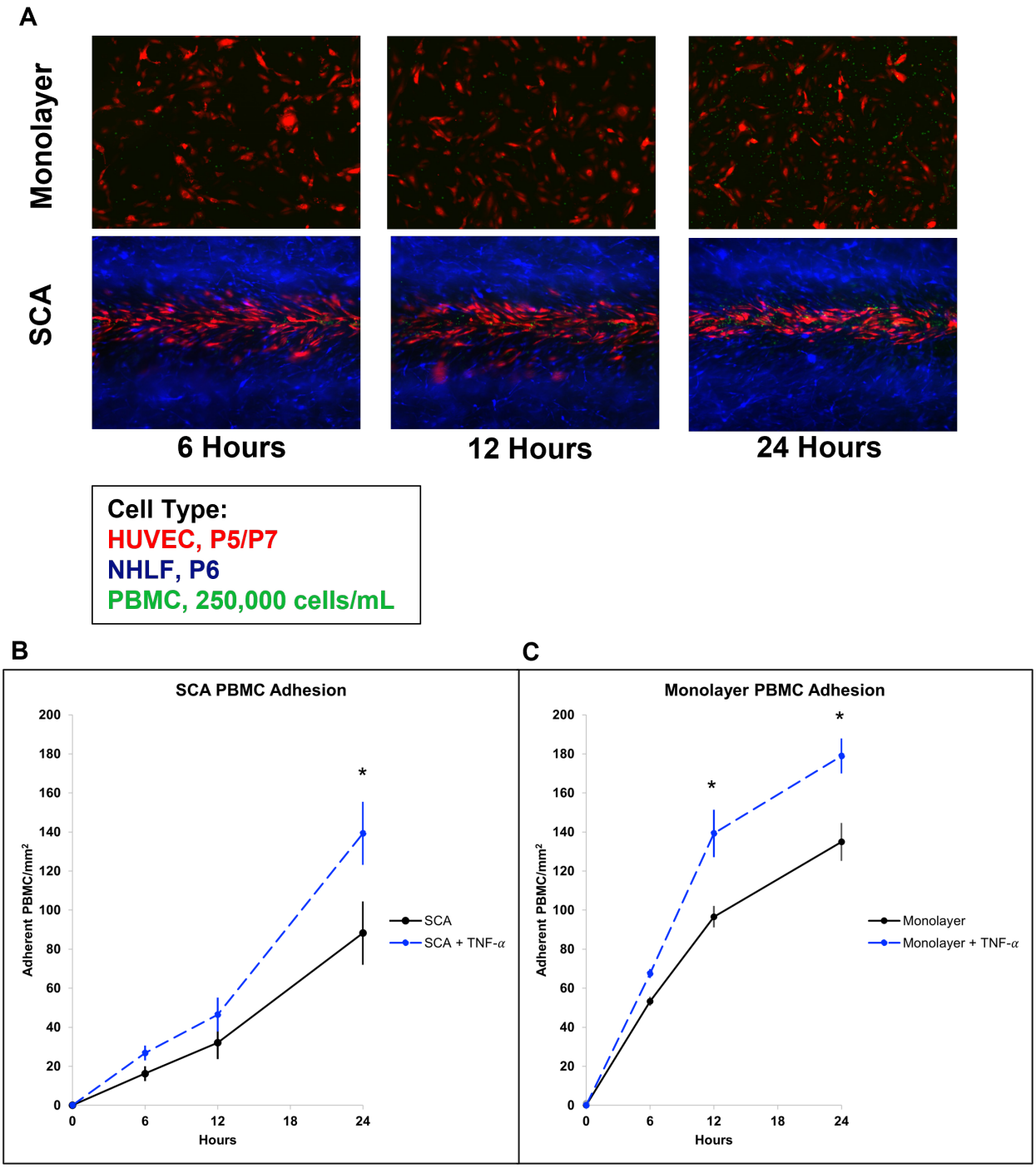

Figure 3. PBMC adhesion in EC monolayer and SCA is augmented by an exogenous inflammatory stimulus. (A) Fluorescent imaging of PBMCs adhering to both EC monolayer and SCA over 24 hours. (B) Quantification of adherent PBMCs to control SCA vessel walls compared to SCA post-TNF-α stimulation. (C) Quantification of adherent PBMCs to control EC monolayer compared to EC monolayer post-TNF-α stimulation. *<0.05

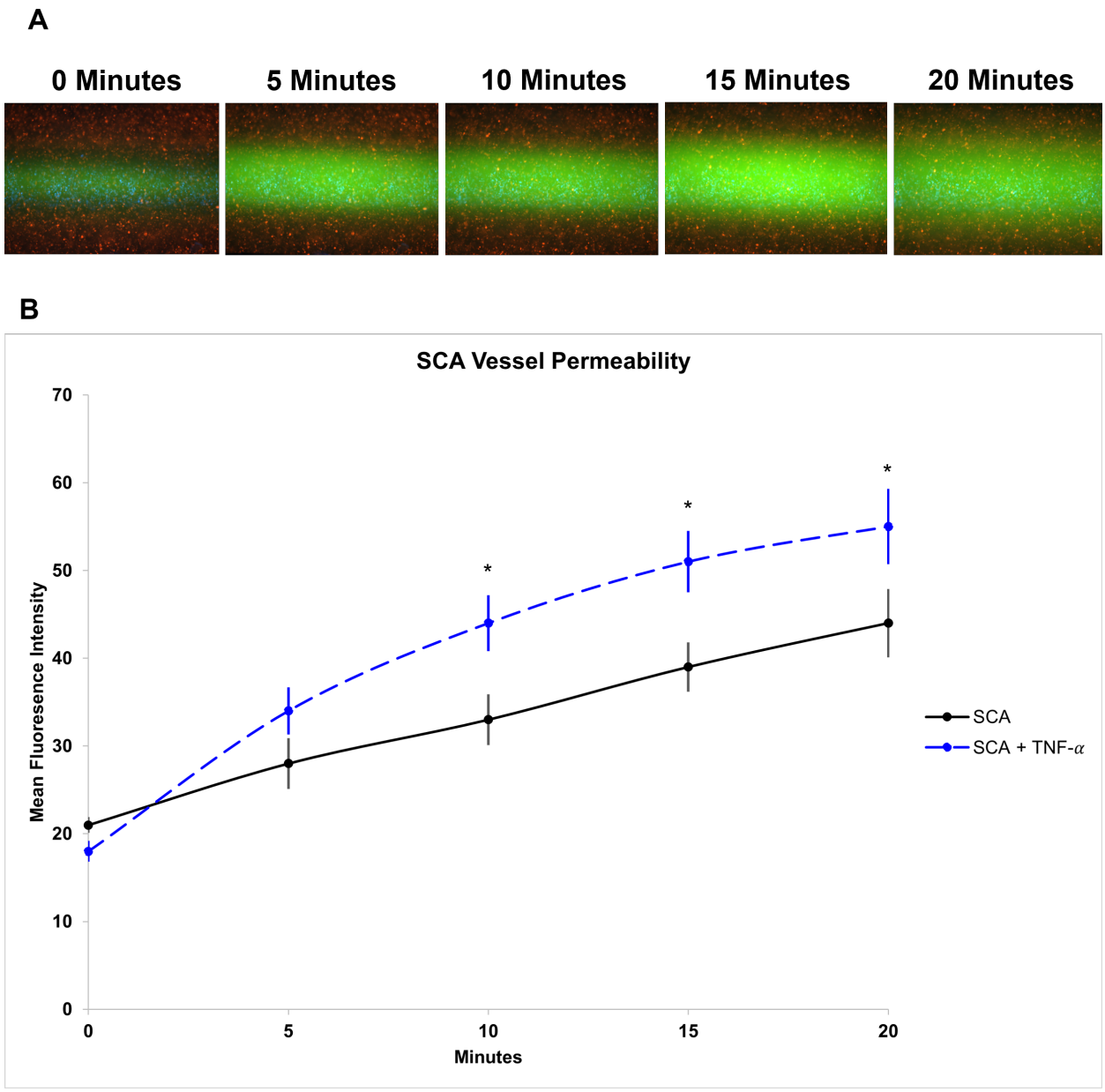

Figure 4. TNF-α induces vascular leak in SCA under flow conditions. (A) Fluorescent imaging over time of SCA with 70 kDa FITC-dextran perfusing through the system. (B) MFI adjacent to vessel wall over 20 min. permeability assay. *<0.05

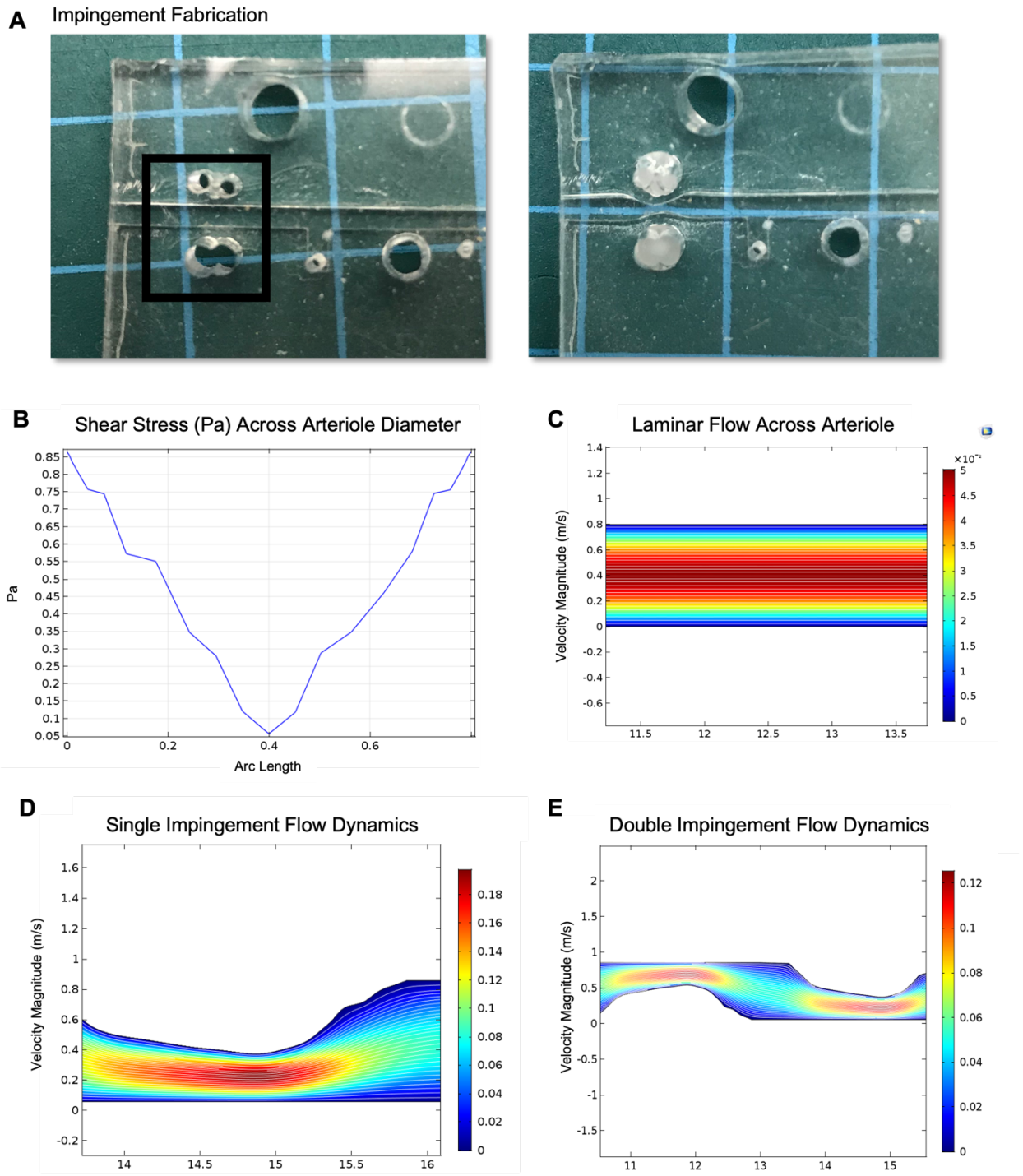

Figure 5. Fabrication and flow dynamics of impinged SCA. (A) Impingement fabrication of SCA devices. Prior to loading of gel-cell mixture holes are punched; following loading polypropylene beads are injected proximal to the tissue chamber displacing the channel wall. (B) Shear stress as a function of location along diameter of the SCA vessel. (C) Laminar flow along SCA vessel length depicted with velocity. (D) Flow velocity perturbations through SCA lumen with single impingement in place. (E) Flow velocity perturbations through SCA lumen with two impingements immediately adjacent.

Discussion

To accurately evaluate leukocyte-endothelium interactions it is critical to recapitulate the *in vivo* factors that contribute to adhesion and transmigration across the endothelial barrier (Sluiter, 1993). Our model provides a promising, novel alternative to current human endothelial cell cultures, significantly improving on monolayer cultures especially. By incorporating microfluidic engineering, we have developed a readily replicable, three-dimensional arteriole organoid that operates within the normal physiological bounds of a *in vivo* arteriole with regards to shear stress and lumen size (An, 2020). Additionally, incorporating fibroblasts in a complex extracellular matrix further improves upon previous models such as Transwell assays where there is mechanical separation of the two distinct cell lines (Justus, 2014). Importantly, fibroblasts are recruited to the developing vessel wall where they differentiate into α-SMA-expressing SMC. The SCA is generated within a relatively short time frame as the combination of cells present in the tissue chamber rapidly adapt to the high shear force present to produce a confluent endothelial cell lumen supported by SMC and stromal fibroblasts.

Upon generation of the fully matured arteriole in the chamber there were distinct morphological and RNA expression pattern differences between the SCA and the same source cell lines in 2D culture, further demonstrating the importance of approximating the complexity of native tissue in the human body. The adhesion and extravasation of leukocytes across the endothelium is a multifactorial process dependent on the expression of adhesion markers, the number of collisions between the two cells, and the priming effect of shear stress on both immune cells and vasculature (Muller, 2003). The SCA can capture these complexities in a controlled microfluidics-based platform. The marked differences between the SCA and 2D assays allows for real-time measurements of the functional phenotype of PBMCs that more accurately model the dynamics of leukocytes in the human body. To better understand the dysregulation of immune cells in vascular tissue there is a growing need for models such as the

SCA that hew closely to the tissue in which the human diseases manifest. CVD and atherogenesis are processes that are highly dependent on shear stress and vessel morphology, the SCA provides an ideal basis to evaluate the initial disease steps that have proved to be elusive to study. We envisage future studies incorporating macrophages and a high lipid load to further develop the SCA as a model for atherosclerosis. The framework for these devices holds great promise for furthering our collective knowledge of atherogenesis as well as other leukocyte-endothelial pathologies, especially critical given the threats posed by the COVID-19 pandemic.

Conclusion

This chapter details the engineering and development of a microfluidic arteriole organoid on a chip that closely mimics the complexities of human vasculature. This robust platform can support a wide range of shear values through the vessel and is dependent on the close interaction between stromal cells and endothelium to develop a functional organoid, both morphologically and regarding expression patterns of key genes. These distinct differences from pre-existing models resulted in significant alterations in leukocyte transmigration across the basement membrane, which is the hallmark of atherogenesis and the basis of CVD. The SCA provides a unique opportunity to visualize and measure the initial stages of chronic disease, potentially allowing for insight into the subtle factors that interplay to result in debilitating end-stage CVD.

References

Allaire, J. (2012). RStudio: integrated development environment for R. *Boston, MA*, *770*(394), 165-171.

Alon, R., & Ley, K. (2008). Cells on the run: shear-regulated integrin activation in leukocyte rolling and arrest on endothelial cells. *Current opinion in cell biology*, *20*(5), 525-532.

An, D., Yu, P., Freund, K. B., Yu, D. Y., & Balaratnasingam, C. (2020). Three-dimensional characterization of the normal human parafoveal microvasculature using structural criteria and high-resolution confocal microscopy. *Investigative Ophthalmology & Visual Science*, *61*(10), 3-3.

Asakura, H., & Ogawa, H. (2021). COVID-19-associated coagulopathy and disseminated intravascular coagulation. *International journal of hematology*, *113*, 45-57.

Auguie, B., Antonov, A., & Auguie, M. B. (2017). Package 'gridExtra'. *Miscellaneous Functions for "Grid" Graphics*.

Barrett-Connor, E., Ayanian, J. Z., Brown, E. R., Coultas, D. B., Francis, C. K., Goldberg, R. J., ... & Mannino, D. M. (2011). A nationwide framework for surveillance of cardiovascular and chronic lung diseases. *Washington DC, USA*.

Bertoni, A. G., Whitt-Glover, M. C., Chung, H., Le, K. Y., Barr, R. G., Mahesh, M., ... & Jacobs, D. R. (2009). The association between physical activity and subclinical atherosclerosis: the Multi-Ethnic Study of Atherosclerosis. *American journal of epidemiology*, *169*(4), 444-454.

Bischoff, J. (2008). Engineering robust and functional vascular networks in vivo with human adult and cord blood–derived progenitor cells. *Circulation research*, *103*(2), 194-202.

Buchanan, C. F., Verbridge, S. S., Vlachos, P. P., & Rylander, M. N. (2014). Flow shear stress regulates endothelial barrier function and expression of angiogenic factors in a 3D microfluidic tumor vascular model. *Cell adhesion & migration*, *8*(5), 517-524.

Bui, T. M., Wiesolek, H. L., & Sumagin, R. (2020). ICAM-1: A master regulator of cellular responses in inflammation, injury resolution, and tumorigenesis. *Journal of Leucocyte Biology*, *108*(3), 787-799.

Copaescu, A., Smibert, O., Gibson, A., Phillips, E. J., & Trubiano, J. A. (2020). The role of IL-6 and other mediators in the cytokine storm associated with SARS-CoV-2 infection. *Journal of Allergy and Clinical Immunology*, *146*(3), 518-534.

Corliss, B. A., Doty, R., Matthews, C., & Peirce, S. M. (2019). REAVER: An Improved Image Analysis Pipeline for Quantifying Microvascular Networks. *The FASEB Journal*, *33*(S1), 525-7.

Crampton, S. P., Davis, J., & Hughes, C. C. (2007). Isolation of human umbilical vein endothelial cells (HUVEC). *Journal of visualized experiments: JoVE*, (3).

Crook, H., Raza, S., Nowell, J., Young, M., & Edison, P. (2021). Long covid—mechanisms, risk factors, and management. *bmj*, *374*.

D'Agostino Sr, R. B., Pencina, M. J., Massaro, J. M., & Coady, S. (2013). Cardiovascular disease risk assessment: insights from Framingham. *Global heart*, *8*(1), 11-23.

Davidson, A. M., Wysocki, J., & Batlle, D. (2020). Interaction of SARS-CoV-2 and other coronavirus with ACE (angiotensin-converting enzyme)-2 as their main receptor: therapeutic implications. *Hypertension*, *76*(5), 1339-1349.

De Jong, M. D., Simmons, C. P., Thanh, T. T., Hien, V. M., Smith, G. J., Chau, T. N. B., ... & Farrar, J. (2006). Fatal outcome of human influenza A (H5N1) is associated with high viral load and hypercytokinemia. *Nature medicine*, *12*(10), 1203-1207.

Dinno, A., & Dinno, M. A. (2017). Package ‘conover. test’. *Conover-Iman test of multiple comparisons using rank*.

Droebner, K., Reiling, S. J., & Planz, O. (2008). Role of hypercytokinemia in NF-κB p50-deficient mice after H5N1 influenza A virus infection. *Journal of virology*, *82*(22), 11461-11466.

Fausto, N. (1998). Atherosclerosis in young people: The value of the autopsy for studies of the epidemiology and pathobiology of disease. *The American Journal of Pathology*, *153*(4), 1021-1022.

Fox, J., Weisberg, S., Adler, D., Bates, D., Baud-Bovy, G., Ellison, S., ... & Monette, G. (2012). Package ‘car’. *Vienna: R Foundation for Statistical Computing*, *16*.

Gibson, P. G., Qin, L., & Puah, S. H. (2020). COVID-19 acute respiratory distress syndrome (ARDS): clinical features and differences from typical pre-COVID-19 ARDS. *Medical Journal of Australia*, *213*(2), 54-56.

Gijsen, F., van der Giessen, A., van der Steen, A., & Wentzel, J. (2013). Shear stress and advanced atherosclerosis in human coronary arteries. *Journal of biomechanics*, *46*(2), 240-247.

Grzegorz Kwiatek
(2023). DXFLib (https://www.mathworks.com/matlabcentral/fileexchange/33884-dxflib), MATLAB Central File Exchange. Retrieved April 20, 2023.

Gunby, P. (1992). Cardiovascular diseases remain nation's leading cause of death. *JAMA*, *267*(3), 335-336.

Gutierrez-Chamorro, L., Riveira-Munoz, E., Barrios, C., Palau, V., Nevot, M., Pedreno-Lopez, S., ... & Ballana, E. (2021). SARS-CoV-2 infection modulates ACE2 function and subsequent inflammatory responses in swabs and plasma of COVID-19 patients. *Viruses*, *13*(9), 1715.

Hachey, S. J., & Hughes, C. C. (2018). Applications of tumor chip technology. *Lab on a Chip*, *18*(19), 2893-2912.

Hamming, I., Timens, W., Bulthuis, M. L. C., Lely, A. T., Navis, G. V., & van Goor, H. (2004). Tissue distribution of ACE2 protein, the functional receptor for SARS coronavirus. A first step in understanding SARS pathogenesis. *The Journal of Pathology: A Journal of the Pathological Society of Great Britain and Ireland*, *203*(2), 631-637.

Hoffmann, M., Kleine-Weber, H., Krüger, N., Müller, M., Drosten, C., & Pöhlmann, S. (2020). The novel coronavirus 2019 (2019-nCoV) uses the SARS-coronavirus receptor ACE2 and the cellular protease TMPRSS2 for entry into target cells. *BioRxiv*, 2020-01.

Hoffmann, M., Kleine-Weber, H., Schroeder, S., Krüger, N., Herrler, T., Erichsen, S., ... & Pöhlmann, S. (2020). SARS-CoV-2 cell entry depends on ACE2 and TMPRSS2 and is blocked by a clinically proven protease inhibitor. *cell*, *181*(2), 271-280.

Hu, B., Huang, S., & Yin, L. (2021). The cytokine storm and COVID-19. *Journal of medical virology*, *93*(1), 250-256.

Insull Jr, W. (2009). The pathology of atherosclerosis: plaque development and plaque responses to medical treatment. *The American journal of medicine*, *122*(1), S3-S14.

Justus, C. R., Leffler, N., Ruiz-Echevarria, M., & Yang, L. V. (2014). In vitro cell migration and invasion assays. *Journal of visualized experiments: JoVE*, (88).

Kahn, R., Robertson, R. M., Smith, R., & Eddy, D. (2008). The impact of prevention on reducing the burden of cardiovascular disease. *Circulation*, *118*(5), 576-585.

Kaneko, N., Satta, S., Komuro, Y., Muthukrishnan, S. D., Kakarla, V., Guo, L., ... & Liebeskind, D. S. Upregulation of ACE2 Expression and its Relationship to Increased Shear Stress: A Protective Mechanism Lost in Cardiovascular Disease.

Kang, S., & Kishimoto, T. (2021). Interplay between interleukin-6 signaling and the vascular endothelium in cytokine storms. *Experimental & Molecular Medicine*, *53*(7), 1116-1123.

Kannel, W. B., & Dawber, T. R. (1972). Atherosclerosis as a pediatric problem. *The Journal of pediatrics*, *80*(4), 544-554.

Kassambara, A. (2020). rstatix: Pipe-friendly framework for basic statistical tests.

Kassambara, A., & Kassambara, M. A. (2020). Package 'ggpubr'. *R package version 0.1*, *6*(0).

Kluge, H. H. P., Wickramasinghe, K., Rippin, H. L., Mendes, R., Peters, D. H., Kontsevaya, A., & Breda, J. (2020). Prevention and control of non-communicable diseases in the COVID-19 response. *The Lancet*, *395*(10238), 1678-1680.

Kong, D. H., Kim, Y. K., Kim, M. R., Jang, J. H., & Lee, S. (2018). Emerging roles of vascular cell adhesion molecule-1 (VCAM-1) in immunological disorders and cancer. *International journal of molecular sciences*, *19*(4), 1057.

Kouhpayeh, H. R., Tabasi, F., Dehvari, M., Naderi, M., Bahari, G., Khalili, T., ... & Taheri, M. (2021). Association between angiotensinogen (AGT), angiotensin-converting enzyme (ACE) and angiotensin-II receptor 1 (AGTR1) polymorphisms and COVID-19 infection in the southeast of Iran: a preliminary case-control study. *Translational medicine communications*, *6*, 1-10.

Lai, B. F. L., Lu, R. X. Z., Davenport Huyer, L., Kakinoki, S., Yazbeck, J., Wang, E. Y., ... & Radisic, M. (2021). A well plate–based multiplexed platform for incorporation of organoids into an organ-on-a-chip system with a perfusable vasculature. *Nature protocols*, *16*(4), 2158-2189.

Lawson, C., & Wolf, S. (2009). ICAM-1 signaling in endothelial cells. *Pharmacological reports*, *61*(1), 22-32.

Le, T. T., Andreadakis, Z., Kumar, A., Román, R. G., Tollefsen, S., Saville, M., & Mayhew, S. (2020). The COVID-19 vaccine development landscape. *Nat Rev Drug Discov*, *19*(5), 305-306.

Ledue, T. B., & Rifai, N. (2003). Preanalytic and analytic sources of variations in C-reactive protein measurement: implications for cardiovascular disease risk assessment. *Clinical Chemistry*, *49*(8), 1258-1271.

Li, W., Moore, M. J., Vasilieva, N., Sui, J., Wong, S. K., Berne, M. A., ... & Farzan, M. (2003). Angiotensin-converting enzyme 2 is a functional receptor for the SARS coronavirus. *Nature*, *426*(6965), 450-454.

Libby, P. (2000). Changing concepts of atherogenesis. *Journal of internal medicine*, *247*(3), 349-358.

Mahmudpour, M., Roozbeh, J., Keshavarz, M., Farrokhi, S., & Nabipour, I. (2020). COVID-19 cytokine storm: The anger of inflammation. *Cytokine*, *133*, 155151.

Melero-Martin, J. M., De Obaldia, M. E., Kang, S. Y., Khan, Z. A., Yuan, L., Oettgen, P., &

Mensah, G. A., & Brown, D. W. (2007). An overview of cardiovascular disease burden in the United States. *Health affairs*, *26*(1), 38-48.

Mohammed, I., Nauman, A., Paul, P., Ganesan, S., Chen, K. H., Jalil, S. M. S., ... & Zakaria, D. (2022). The efficacy and effectiveness of the COVID-19 vaccines in reducing infection, severity, hospitalization, and mortality: A systematic review. *Human vaccines & immunotherapeutics*, *18*(1), 2027160.

Moya, M. L., Hsu, Y. H., Lee, A. P., Hughes, C. C., & George, S. C. (2013). In vitro perfused human capillary networks. *Tissue Engineering Part C: Methods*, *19*(9), 730-737.

Muller, W. A. (2003). Leukocyte–endothelial-cell interactions in leukocyte transmigration and the inflammatory response. *Trends in immunology*, *24*(6), 326-333.

Munro, J. M. (1993). Endothelial-leukocyte adhesive interactions in inflammatory diseases. *European heart journal*, *14*, 72-77.

Murrell, P. (2002). The grid graphics package. *R News*, *2*(2), 14-19.

Palmefors, H., DuttaRoy, S., Rundqvist, B., & Börjesson, M. (2014). The effect of physical activity or exercise on key biomarkers in atherosclerosis–a systematic review. *Atherosclerosis*, *235*(1), 150-161.

Phan, D. T., Wang, X., Craver, B. M., Sobrino, A., Zhao, D., Chen, J. C., ... & Hughes, C. C. (2017). A vascularized and perfused organ-on-a-chip platform for large-scale drug screening applications. *Lab on a Chip*, *17*(3), 511-520.

Potus, F., Mai, V., Lebret, M., Malenfant, S., Breton-Gagnon, E., Lajoie, A. C., ... & Provencher, S. (2020). Novel insights on the pulmonary vascular consequences of COVID-19. *American Journal of Physiology-Lung Cellular and Molecular Physiology*, *319*(2), L277-L288.

Radom-Aizik, S., Zaldivar Jr, F., Oliver, S., Galassetti, P., & Cooper, D. M. (2010). Evidence for microRNA involvement in exercise-associated neutrophil gene expression changes. *Journal of applied physiology*, *109*(1), 252-261.

Radom-Aizik, S., Zaldivar Jr, F., Leu, S. Y., Adams, G. R., Oliver, S., & Cooper, D. M. (2012). Effects of exercise on microRNA expression in young males peripheral blood mononuclear cells. *Clinical and translational science*, *5*(1), 32-38.

Rafieian-Kopaei, M., Setorki, M., Doudi, M., Baradaran, A., & Nasri, H. (2014). Atherosclerosis: process, indicators, risk factors and new hopes. *International journal of preventive medicine*, *5*(8), 927.

Ramasamy, S., & Subbian, S. (2021). Critical determinants of cytokine storm and type I interferon response in COVID-19 pathogenesis. *Clinical microbiology reviews*, *34*(3), e00299-20.

Ritz, C., Baty, F., Streibig, J. C., & Gerhard, D. (2015). Dose-response analysis using R. *PloS one*, *10*(12), e0146021.

ROBERTS JR, J. C., MOSES, C., & WILKINS, R. H. (1959). Autopsy studies in atherosclerosis: I. Distribution and severity of atherosclerosis in patients dying without morphologic evidence of atherosclerotic catastrophe. *Circulation*, *20*(4), 511-519.

Roberts, K. A., Colley, L., Agbaedeng, T. A., Ellison-Hughes, G. M., & Ross, M. D. (2020). Vascular manifestations of COVID-19–thromboembolism and microvascular dysfunction. *Frontiers in cardiovascular medicine*, *7*, 598400.

Rosas, I. O., Bräu, N., Waters, M., Go, R. C., Hunter, B. D., Bhagani, S., ... & Malhotra, A. (2021). Tocilizumab in hospitalized patients with severe Covid-19 pneumonia. *New England Journal of Medicine*, *384*(16), 1503-1516.

Ross, R. (1986). The pathogenesis of atherosclerosis—an update. *New England journal of medicine*, *314*(8), 488-500.

Roux, E., Bougaran, P., Dufourcq, P., & Couffinhal, T. (2020). Fluid shear stress sensing by the endothelial layer. *Frontiers in Physiology*, *11*, 861.

Schindelin, J., Arganda-Carreras, I., Frise, E., Kaynig, V., Longair, M., Pietzsch, T., ... & Cardona, A. (2012). Fiji: an open-source platform for biological-image analysis. *Nature methods*, *9*(7), 676-682.

Sluiter, W., Pietersma, A., Lamers, J. M., & Koster, J. F. (1993). Leukocyte adhesion molecules on the vascular endothelium: their role in the pathogenesis of cardiovascular disease and the mechanisms underlying their expression. *Journal of cardiovascular pharmacology*, *22*, S37-44.

Sobrino, A., Phan, D. T., Datta, R., Wang, X., Hachey, S. J., Romero-López, M., ... & Hughes, C. C. (2016). 3D microtumors in vitro supported by perfused vascular networks. *Scientific reports*, *6*(1), 31589.

Song, J., Hu, B., Qu, H., Wang, L., Huang, X., Li, M., & Zhang, M. (2020). Upregulation of angiotensin converting enzyme 2 by shear stress reduced inflammation and proliferation in vascular endothelial cells. *Biochemical and Biophysical Research Communications*, *525*(3), 812-818.

Stein, J. H., Korcarz, C. E., Hurst, R. T., Lonn, E., Kendall, C. B., Mohler, E. R., ... & Post, W. S. (2008). Use of carotid ultrasound to identify subclinical vascular disease and evaluate cardiovascular disease risk: a consensus statement from the American Society of Echocardiography Carotid Intima-Media Thickness Task Force endorsed by the Society for Vascular Medicine. *Journal of the American Society of echocardiography*, *21*(2), 93-111.

Strong, J. P., & McGill Jr, H. C. (1969). The pediatric aspects of atherosclerosis. *Journal of atherosclerosis research*, *9*(3), 251-265.

Takeishi, N., Imai, Y., Nakaaki, K., Yamaguchi, T., & Ishikawa, T. (2014). Leukocyte margination at arteriole shear rate. *Physiological reports*, *2*(6), e12037.

Tang, Y., Liu, J., Zhang, D., Xu, Z., Ji, J., & Wen, C. (2020). Cytokine storm in COVID-19: the current evidence and treatment strategies. *Frontiers in immunology*, *11*, 1708.

Turner, N. A., & Moake, J. L. (2015). Factor VIII is synthesized in human endothelial cells, packaged in Weibel-Palade bodies and secreted bound to ULVWF strings. *PloS one*, *10*(10), e0140740.

Wickham, H. (2011). ggplot2. *Wiley interdisciplinary reviews: computational statistics*, *3*(2), 180-185.

Xiao, Y., & Torok, M. E. (2020). Taking the right measures to control COVID-19. *The Lancet Infectious Diseases*, *20*(5), 523-524.

Xu, J., Lupu, F., & Esmon, C. T. (2010). Inflammation, innate immunity and blood coagulation. *Hämostaseologie*, *30*(01), 5-9.

Xu, S. W., Ilyas, I., & Weng, J. P. (2023). Endothelial dysfunction in COVID-19: an overview of evidence, biomarkers, mechanisms and potential therapies. *Acta Pharmacologica Sinica*, *44*(4), 695-709.

Zudaire, E., Gambardella, L., Kurcz, C., & Vermeren, S. (2011). A computational tool for quantitative analysis of vascular networks. *PloS one*, *6*(11), e27385.